December 5, 2016

MASTER THESIS - **CONFIDENTIAL**

Development of an optimisation process for pre-swirl stator designs

B. Feldbrugge

Faculty of Engineering Technology
Mechanical Engineering
Engineering Fluid Dynamics

Exam committee:
Prof.dr.ir. C.H. Venner
Ir. B. Schuiling
Dr. ir. N.P. Kruyt
Ir. J.P. Schilder

Documentnumber
EFD — 249

MARIN

UNIVERSITY OF TWENTE.

Development of an optimisation process for pre-swirl stator designs

For obtaining the degree of Master of Science in Mechanical Engineering at University of Twente

Wageningen
December 5, 2016

Berend Feldbrugge
University of Twente
Marin

Engineering Fluid Dynamics
Faculty of Engineering Technology
University of Twente

Summary

A pre-swirl stator is a tool to reduce a ship's propulsion power, resulting in more sustainable transport of goods at lower costs. Previous research has shown that a 7% reduction of the propulsive power is possible, saving up to $84.000 and 540 MT CO_2 a year for an average cargo ship. With a pre-swirl stator, the flow field towards the propeller can be changed in a favourable way. This allows the propeller to have a lower rotation rate with constant net-thrust of the propeller. Due to the lower rotation rate of the propeller, the rotational velocity components in the wake behind the ship are reduced; losses due to rotational kinetic energy left in the wake decrease.

In this research, an optimisation tool is developed to optimise the pre-swirl stator geometry in open water, i.e. homogeneous distributed axial inflow. This tool uses a Single Objective Genetic Algorithm (SOGA) and is tested for two different sets of design parameters. Also, different generation sizes and different number of generations are tested. The effect of the pre-swirl stator on the propeller is simulated with Computational Fluid Dynamics (CFD) which calculates the velocity and pressure around the pre-swirl stator and propeller with a Boundary Element Method (BEM). With this method, calculation times are short, though at the cost of a less detailed flow field description.

The optimisation objective is to find the minimum required power to generate a given thrust. Optimal designs show a power reduction of 5.3-6.5% and a parameter study showed that the pitch angle of the pre-swirl stator is the main design parameter to vary in an optimisation. It has a larger influence on the power compared to the chord or the camber of the pre-swirl stator blades. Comparison of the flow field of a propeller with and without pre-swirl stator showed a difference in both tangential and axial forces, which is increased over a large part of the propeller blade. The pressure distribution was changed mainly at lower radial sections, where the lift coefficient increased for the propeller with stator.

A comparison of results from the BEM code is made with results from a more detailed Reynolds Averaged Navier-Stokes simulation. Differences were found in the prediction of the friction force and the power, which could be a topic of further research. Overall, with the optimisation tool developed in this research, a new step is taken to improve the design process and effect of a pre-swirl stator for ships.

Contents

Nomenclature

List of abbreviations

AAXL	Additional Axial Losses
BEM	Boundary Element Method
CFD	Computational Fluid Dynamics
DOF	Degree Of Freedom
DWT	Dead Weight Tonnage
ESD	Energy Saving Devices
GRIP	Green Retrofitting through Improved Propulsion
IAXL	Ideal Axial Losses
PDE	Partial Differential Equation
PNS	Propeller without stator
PWD	Propeller with stator
RMSE	Root Mean Squared Error
ROTL	Rotational Losses
TAXF	Total Axial Losses

List of symbols

T_{prop}	Propeller target thrust	[N]
$\dot{Q}$	Rate of volumetric heating	[W/m^3]
η_h	Hull efficiency	[-]
η_r	Relative rotative efficiency	[-]
η_i	Ideal efficiency	[-]
η_p	Propeller open water efficiency	[-]
Γ	Circulation	[m^2/s]

μ	Viscosity	[Pa s]
ω_i	Angular velocity of the propeller blade	[rad/s]
∂V	Control volume surface	[m^2]
∂V_p	Control volume propeller surface	[m^2]
∂V_v	Control volume outer surface	[m^2]
ρ	Density	[kg/m^3]
τ_{ij}	Viscous stress tensor	[Pa]
A	Surface	[m^2]
D	Propeller diameter	[m]
dJw	Advance coefficient difference	[-]
dp	Pressure difference	[Pa]
dV	Velocity difference	[m/s]
E	Energy	[W/m^2]
E_r	Radial kinetic energy flux	[kw/m^2]
E_t	Tangential kinetic energy flux	[kw/m^2]
E_x	Axial kinetic energy flux	[kw/m^2]
E_{int}	Internal energy	[W/m^2]
E_{kin}	Kinetic energy	[W/m^2]
E_{pot}	Potential energy	[W/m^2]
f_i	Body force	[N]
g	Gravitational acceleration	[m/s^2]
J	Advance coefficient	[-]
J_{act}	Actual Advance Coefficient	[-]
K_q	Torque coefficient	[-]
K_t	Thrust coefficient	[-]
L	Lift	[N]
l_{ref}	Reference length	[m]
n	Propeller rotation rate	[rev/s]
n_i	Outward unit normal	[-]
n_w	Rotation rate of the wake	[rev/s]
p	Pressure	[Pa]
P_d	Power delivered at the shaft	[W]

p_{atm}	Atmospheric pressure	[Pa]
P_{eff}	Effective power	[W]
P_{ow}	Power open water simulations	[W]
Q	Torque	[Nm]
q_i	Heat flux vector	[W/m^2]
Q_{ow}	Torque open water simulations	[N]
R	Hull resistance	[N]
r_i	Vector of distance wit respect to origin	[m]
r_{hub}	Radius propeller hub in Procal	[-]
r_{tip}	Radius propeller tip in Procal	[-]
Re	Reynolds nuber	[-]
T	Thrust	[N]
t	Thrust deduction factor	[-]
t	Time	[s]
T_{nett}	Netto thrust	[N]
T_{ow}	Thrust open water simulations	[N]
T_{stat}	Stator thrust	[N]
U	Uncertainty percentage	[-]
u_i	Velocity vector	[m/s]
u_i^{rel}	Relative velocity vector	[m/s]
V	Control volume	[m^3]
V	Velocity	[m/s]
V_s	Ship velocity	[m/s]
v_t	Tangential velocity in Procal	[-]
V_{ad}	Speed of advance of the propeller	[-]
V_d	Ship design speed	[knots]
$v_{x,prop}$	Axial velocity propeller wake field	[-]
w	Wake fraction	[-]

Chapter 1

Introduction

Whether it is for recreation of for transport, ships can be found all over the world. Especially when it comes to transport, they play an important role. For example, over the year 2014 the total amount of cargo (oil, gas, bulk and other dry cargo) transported as part of international seaborne trade was 9.8 billion tons [2]. To carry out this transport, billions of tonnes of fuel are burned. This has a big impact on the environment, and also causes high costs to operate ships.

In general, cargo ships like depicted in fig. 1.1 are driven by a propeller, which can be spotted at the left bottom in this picture. The propeller transfers the rotational motion from the combustion engine to linear movement of the ship, which will induce losses always. However, it is possible to reduce these losses using an energy saving device (ESD).

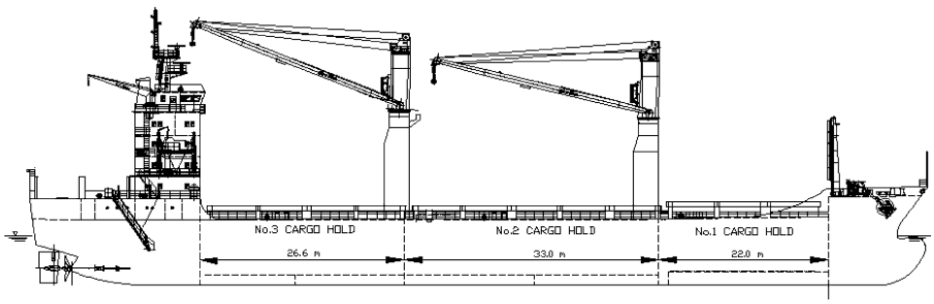

Figure 1.1: Side view of an cargo ship [1].

The development of ESDs for ships have been a topic of researches since the early 1980s. In general, an energy saving device is mounted on a ship in the vicinity of the propeller, resulting in reduction of fuel costs and emissions. There are many different types of ESD's, such as ducts, stator fins, rudder bulbs or combinations of these options. For an example of a certain type of stator fins, see fig. 1.2. This figure shows a schematic overview of a pre-swirl stator, or simply stator. In this research, an optimisation tool is developed in order to optimise the design of pre-swirl stators.

During the oil crisis in the 1980s, research projects were initiated to develop ESD's. Some of these where actually tested in full scale trials, however, only a few where developed

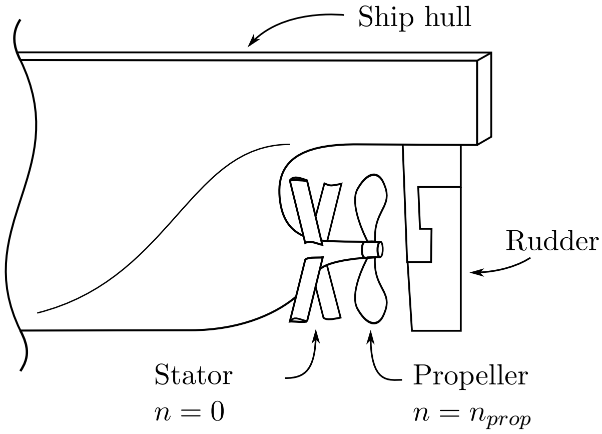

Figure 1.2: Sketch of ship hull at the stern section. A pre-swirl stator is fixed to the hull right in front of the propeller.

further as the urge to save fuel decreased. Later, around 2010 due to high oil prices, new interest arose to increase the propulsive efficiency of ships. Also governmental and public pressure to improve the sustainability of shipping gave an incentive to further develop ESD's. Currently, the effects and influence of ESD's can be studied in greater detail using Computational Fluid Dynamics (CFD) software. Using these tools, research and development costs are reduced compared to the experiments and tests in the early days.

An ESD is intended to improve the propulsive efficiency of a ship, which can be defined after identification of the propulsive losses. Propulsive losses can roughly be subdivided in axial losses, rotational losses and frictional losses, which take 35-40% of the propulsive power all together [7]. A pre-swirl stator mainly reduces the rotational losses by creating rotation in the wake field in front of the propeller. Tests and simulations done so far generally show energy saving percentages of 5%, although higher percentages have been found as well.

Assumed 7% reduction of fuel consumption would be accomplished, a pre-swirl stator installed on an general cargo vessel of 25,000 DWT (Dead Weight Tonnage), will save approximately 175 MT fuel a year. This results in an annual save of roughly $84,000 and 540 MT CO_2 [5].

For Marin, further development of this technology is important. Marin was involved in a European project on Green Retrofitting trough Improved Propulsion (GRIP) several years back. As part of this project, a blade improving stator duct was designed and tested for a ship with a fixed pitch propeller, sailing under design conditions [4]. A blade improving stator duct is a kind of pre-swirl stator, where the tip of the stator fins are attached to each other by a duct. With the knowledge gained in this project, Marin aims to improve its capabilities to create a reliable and efficient ESD design, partly to offer as a service to future customers and partly to use in a new project as follow up on GRIP. An optimisation routine would help to create the best stator design faster, reducing development costs making it more attractive for shipping companies to use a stator. This in turn saves money and contributes to a more sustainable transport over seas.

1.1 Problem definition

The research and development of pre-swirl stators done so far has shown promising results; the working principles and global geometry of pre-stators are known and a considerable power reduction is proved to be possible. However, in order to improve the designs, more detailed information about the influence of different design parameters is necessary. Right now, designing a stator is a slow and iterative process, where the designer simulates different designs and tries to find the best shape manually. To increase the speed of this process, and to improve the effect of a pre-stators further, an optimisation tool would be very useful.

Optimisation is a process "to improve the design so as to achieve the best way of satisfying the original need, within the available means" [3]. With an optimisation tool, a larger set of design parameters can be tested compared to the manual testing. However, for an increasing number of optimisation variables the number of simulations will increase too. In order to keep calculation time and costs low, a potential flow solver is used to perform the simulations. This kind of simulation allows for fast calculations at the expense of solving a simplified set of flow equations. Still, using such a solver, a good solution can be obtained, which makes it suitable to use in an optimisation process. The design, obtained from the optimisation, is further investigated using viscous flow solvers, which model the flow with more detail.

At Marin, the software and knowledge to do optimisation and to do potential flow simulations are all available. However, the optimisation and simulation methods are not linked to each other. The aim of this research is to develop an interface which makes this link.

1.2 Research question

With above information in mind, the main question of this research is posed as:

How can MARIN's numerical simulation tools be merged into an optimisation framework for pre-swirl stators, in order to lower the required power of a ships propeller operating in open water?

To get to the final answer, three sub-questions are posed which will be answered in the course of this report:

- *What are the design parameters of a pre-swirl stator?*
- *What is a suitable optimisation routine given the software available at Marin?*
- *What is the effect of a pre-swirl stator on the propulsive efficiency of a propeller?*

In the course of the report, these questions will be discussed. Also they will be recapitulated in the conclusion.

Chapter 2

Background

This research will focus on reducing fuel consumption of ships by improving the performance of the propeller with a pre-swirl stator. A short introduction is given to explain the theory behind ship propulsion, which is explained from the theory of an ideal propulsor and the conventional expression for propeller efficiency. Using the first law of thermodynamics (conservation of energy), important losses are identified.

After this section, the effect of pre-swirl on the propeller is discussed. A link to the propeller losses, defined in the first section, is made and the energy balance is determined for the stator. The effect of a pre-swirl stator is visualised by a graph, relating the kinetic energy of the wake rotation to the change of power needed to generate a constant thrust. Finally, a definition for the efficiency of a stator will be given.

2.1 Theory of propulsion

When a ship sails with a steady forward speed through the water, it is subjected to a resistance force pointing in aft direction. Resistance is a result of frictional and pressure forces of water and air acting on the hull. In order to overcome this resistance, an propelling "thrust" force needs to be applied, which enables the ship to keep its constant velocity. The purpose of a propeller is to generate thrust, converting the rotational motion generated by a motor to a linear motion of the ship. As will be explained in this section, this will introduce certain losses, which are derived from the energy conservation law. Yet, to explain the working principle of propulsion, the concept of an actuator disk is discussed.

2.1.1 Actuator disk

The concept of an actuator disk, or ideal propulsor, is a simplification of a propeller. It is a description similar to the momentum theory, which is applied in, for example, the aerodynamic theory behind wind turbines [9]. In the present case, the finite number of propeller blades are replaced by a simple disk which acts on the flow by means of a pressure difference. An actuator disk would be the most efficient way to generate thrust as the energy supplied to the system is fully converted to thrust. However, the efficiency of an actuator disk is not 100%, which is an important effect when considering propulsion.

Imagine a virtual disk with surface (A) in a homogeneous distributed axial flow with velocity V and pressure p. The disk acts on the flow by means of a positive pressure difference (dp) in stream wise direction, as depicted in fig. 2.1. The pressure difference results in a thrust force T, acting on the disk pointing in opposite direction of the flow with magnitude $T = dpA$.

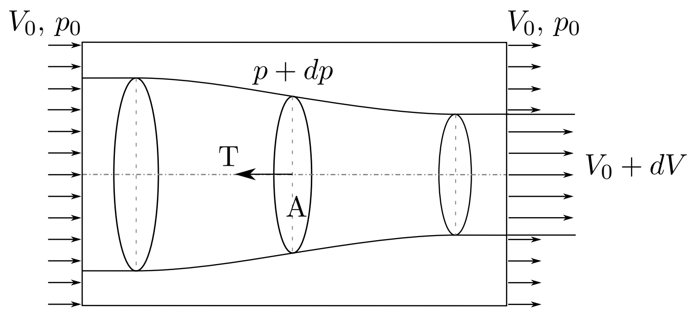

Figure 2.1: Schematic representation of a virtual disk.

The thrust generated causes an acceleration of the flow, which results in a velocity difference (dV). This is the very reason for the actuator disk efficiency not being 100%. Due to the increased velocity, the kinetic energy in the outflow of the disk is higher compared to the kinetic energy at the inflow. In order to quantify the efficiency of the actuator disk, or the ideal efficiency, the work done by thrust is related to the energy which is added to the slipstream. The work done by thrust is the product of thrust with the advance velocity of the actuator disk, i.e. $P_{eff} = TV$, while the energy added to the flow equals $P_d = T(V + dv)$.

$$\begin{aligned}\eta_i &= \frac{P_{eff}}{P_d} \\ &= \frac{TV}{T(V+dv)}\end{aligned} \tag{2.1}$$

Or, alternatively, the ideal efficiency can be defined in terms of the energy lost. For an actuator disk these losses are called Ideal Axial Losses (IAXL).

$$\begin{aligned}\eta_i &= \frac{P_d - IAXL}{P_d} \\ &= 1 - \frac{IAXL}{P_d}\end{aligned} \tag{2.2}$$

In fig. 2.1 the flow streamlines are drawn, showing contraction of the flow. Conservation of mass requires the flow to converge to a relative smaller cross section due to the acceleration of the flow. For a larger thrust loading, and therefore a larger pressure difference, the effect of contraction will increase, as does the velocity difference in the slipstream. Equation (2.1) shows that the efficiency is related to the velocity difference in the slipstream in a reverse way, while the velocity difference is related directly to the pressure difference over the disk. For increasing disk size the pressure difference will decrease evenly while the generated thrust remains constant. This leads to the conclusion that it is beneficial to use the largest size disk possible.

2.1.2 Propulsive efficiency

From the ideal efficiency, the next step is to analyse the propulsive efficiency. In classical naval architecture, the performance of a propeller is defined using its open water performance, corrected for the interaction with the hull. When a propeller operates in open water, it is subjected to a homogeneous axial inflow, without any fluctuations in flow velocity and pressure due to the presence of a hull. The interaction of the propeller with the hull is defined by the wake fraction, w, and the thrust deduction factor, t.

$$\begin{aligned} w &= 1 - \frac{V_{ad}}{V} \\ t &= \frac{T-R}{T} \end{aligned} \tag{2.3}$$

The wake fraction is defined by the fraction of the actual velocity at the propeller, or the advance velocity, V_{ad}, over the velocity of the ship, V. The thrust deduction factor is an expression which relates the resistance of the hull, R, to the generated thrust, T, at constant speed. A propeller induces pressure differences at the aft part of the hull, changing the resistance of the ship from the measured resistance [10]. The propulsive efficiency is defined by measures of the thrust (T) and torque (Q) for both open water and in behind conditions, combined with the ship velocity, as given below. In this equation, open water parameters are indicated by the indices 'o'.

$$\begin{aligned} \eta_D &= \frac{T_o V(1-w)}{2\pi Q_o n} \frac{Q_o T}{T_o Q} \frac{1-t}{1-w} \\ &= \eta_p \eta_r \eta_h \end{aligned} \tag{2.4}$$

In this definition, η_p is the propeller efficiency in open water, η_r the relative rotative efficiency and η_h the hull efficiency. However, this description is useless when quantifying the efficiency improvement due to a pre-swirl stator. In order to get to a suitable description of improvement using a stator it is important to have insight in the different loss components of a propeller.

As explained above, the actuator disk is a simplified version of a propeller, acting on the flow by creating a pressure difference. Even in the ideal situation, with the actuator disk, losses occur; ideal axial losses. In case of a real propeller four extra losses are introduced:

- Rotational losses,
- Viscous losses,
- Losses due to the finite number of blades,
- Losses as a result of non-optimum radial load distribution.

While the actuator disk performs work in a purely axial direction, the propeller does not. The total force on the blade is generated almost perpendicular to the propeller blade, so with the blades placed under a certain pitch angle a rotative component is introduced. This effect occurs especially at the lower radial sections where the blade pitch is typically larger.

Second, Viscous losses are a result of friction and drag due to surface roughness. These losses occur mainly at the larger radial sections of the propeller blade, where velocity is relative high compared to the lower radial sections.

The third loss term can be explained from the wake field distribution. With a finite number of blades, it is impossible to accelerate the flow uniformly as done by the actuator disk. This results in a non-uniform distribution of the induced velocity and hence in an increase of kinetic energy, which is carried away in the slipstream. Also a non-optimum load distribution, the fourth loss term, results in non-uniform induced velocities and hence in an additional loss of energy. With these loss terms in mind it would be beneficial to increase the number of blades, however, this will increase the losses due to the viscous effects.

The different loss terms can be identified using the conservation of energy equation. This way more insight is gained in the different losses introduced by a propeller and how these might be reduced.

2.1.3 Energy analysis propeller

The governing equations in fluid dynamics are defined by three conservation laws: Conservations of mass, momentum and energy. From these laws, the latter can be analysed to get more acquainted with propeller losses [7]. Conservation of energy states that the time rate change of the total energy in a system must equal the sum of net heat fluxes into the system and rate of work done on the system due to body- and surface forces. This equation is valid in case the flow is uniform and homogeneous distributed. In order to describe the system, an arbitrary control volume $V(x_i)$ is defined, depicted in fig. 2.2. The control volume boundary is a closed surface $\partial V(x_i)$, where n_i is the unit normal vector relative to this surface, pointing out of the volume. The vector $u_i(x_i,t)$ is the local velocity vector, depending on the location and time.

$$\begin{aligned}\frac{d}{dt}\iiint\limits_V \rho E dV + \iint\limits_{\partial V} \rho E(u_i n_i) dS = \iiint\limits_V f_i u_i dV - \iint\limits_{\partial V} p(u_i n_i) dS \\ + \iint\limits_{\partial V} (\tau_{ij} u_i) n_j dS + \iiint\limits_V \dot{Q} dV - \iint\limits_{\partial V} q_i n_i dS\end{aligned} \tag{2.5}$$

In this equation E denotes the total energy per unit mass, which is defined as the sum of the kinetic energy, E_{kin}, the potential energy, E_{pot} and the internal energy, E_{int}.

$$E = E_{kin} + E_{pot} + E_{int} \tag{2.6}$$

The two terms on the left hand side of eq. (2.5) express the change of total energy over time and the amount of energy which is transported over the bounding surface. In case

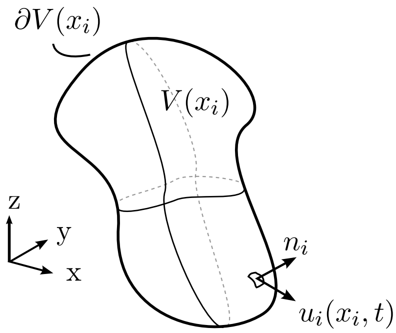

Figure 2.2: Arbitrary control volume $V(x_i)$.

of the propeller system, the former accounts for difference in the wake field over time, which can be neglected in case of open water simulations. The latter term describes the convection of energy over the system bounding surface per unit time.

On the right hand side, two groups of terms can be distinguished. The two last terms account for the head added to the system, where $\dot{Q}$ describes the volumetric heating while q_i stand for the heat flux vector. However, it can be assumed no thermal heat is conducted within or transported into the system, so the last two terms of eq. (2.5) are neglected.

The three remaining terms on the right hand side of the energy equation corresponds to the work per unit of time, carried out by the surface and body of the control volume on its surroundings. The first term describes the work done by body forces, f_i, such as gravity or electro magnetic forces. As gravity does not perform any work on the propeller and control volume, and no other external body forces are applied, this term is neglected. The second term accounts for the work done by pressure, p, and the third term describes friction forces, where τ_{ij} is the viscous stress tensor for Newtonian fluids. The simulations, performed in this research, use a potential flow solver. This solver does not take viscous effects in account in its main process, it only corrects for it in the post-process. For the sake of convenience, viscosity is neglected in this analysis.

In short, when regarding a propeller in open water, time dependent effects can be neglected, as are the influences due to transport or conduction of heat, external body forces and viscosity. These assumptions simplify expression of energy and the energy equation, which boils down to the equation printed below.

$$
\begin{gathered}
E = E_{kin} = \frac{1}{2}||u_i||^2 \\
\iint\limits_{\partial V} \frac{1}{2}\rho||u_i||^2(u_i n_i)dS + \iint\limits_{\partial V} p(u_i n_i)dS = 0
\end{gathered}
\tag{2.7}
$$

The control volume regarded in this case is a cylinder fitted closely around the propeller with an inlet domain some distance upstream and an exit domain some distance downstream of the propeller, fig. 2.3. In order to make a distinction between the power added to the flow by the propeller, and how this power is transferred to the surrounding, the surface of this volume is subdivided in two components: The control volume outer surface (∂V_v) and the propeller surface (∂V_p).

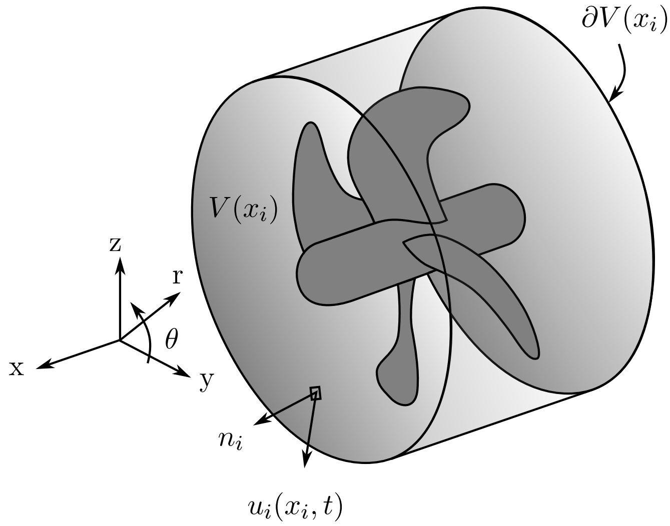

Figure 2.3: Propeller control volume.

From the definition of propulsive efficiency in eq. (2.4), the expression for the delivered power can be derived, $P_d = 2\pi n Q$. This should be equal to the work applied by the propeller on the flow, i.e. the power flux over the propeller surface ∂V_p, which is related to the velocity from an absolute frame of reference. This absolute velocity (u_i) is defined as the sum of the flow velocity while travelling with the blade (u_i^{rel}) and the velocity due to rotation of the blade ($\omega_i \times r_i$).

$$u_i = u_i^{rel} + \omega_i \times r_i \tag{2.8}$$

In above equation, $\omega_i = (2\pi n, 0, 0)^T$, which defines the angular velocity of the propeller blade and r_i is the vector defining the distance with respect of the origin. Since the propeller blades are impermeable, the inner product of the relative velocity is equal to zero, this results in the following expression for the power delivered by the propeller

$$\begin{aligned} P_d &= \iint\limits_{\partial V_p} \frac{1}{2}\rho||(\omega_i \times r_i)||^2((\omega_i \times r_i)\cdot n_i)dS + \iint\limits_{\partial V_p} p((\omega_i \times r_i)\cdot n_i)dS \\ &= 2\pi Q n \end{aligned} \tag{2.9}$$

Next, axial losses are identified from the total axial fluxes (TAXF). The total axial fluxes are defined as the sum of work by pressure and the work due to the change in axial velocity. With the control volume outer surface located close to the propeller, pressure performs work on the outer surface, which is troublesome as this contribution acts in both axial and radial direction. In [7] it was shown that this work mainly contributes to the axial kinetic energy flux and not to the rotational energy flux. Hence it is assumed that the work by pressure over the outer surface can be added to the axial energy fluxes.

$$TAXF = \iint\limits_{\partial V_v} \frac{1}{2}\rho u_x^2(u_i n_i)dS + \iint\limits_{\partial V_v} p(u_i n_i)dS \tag{2.10}$$

The total axial velocity can be divided in three components, the effective power (P_{eff}), ideal axial losses (IAXL) and additional axial losses (AAXL). The former two are discussed in section 2.1.1 and are used to obtain the additional axial losses. The latter describes the losses as a result of the propeller having a finite number of blades, discussed in section 2.1.2. Note that the derivation of the ideal- and additional axial losses only hold in case the propeller is operated in open water. For a propeller operating in behind, the ideal efficiency will be different.

$$\begin{aligned} P_{eff} &= TV \\ IAXL &= \left(1 - \frac{1}{\eta_i}\right) P_{eff} \\ AAXL &= TAXF - P_{eff} - IAXL \end{aligned} \tag{2.11}$$

The remaining term in the simplified equation for energy conservation denote the rotational losses. Both the tangential and radial velocity are assigned to the rotational losses as neither of them contribute to the thrust in an effective way.

$$ROTL = \iint\limits_{\partial V_v} \frac{1}{2}\rho(u_r^2 + u_\theta^2)(u_i n_i) dS \tag{2.12}$$

Summarising, the conservation of energy eq. (2.7), defined in terms of the different components reeds:

$$P_d = P_{eff} + IAXL + AAXL + ROTL \tag{2.13}$$

As discussed in section 2.1.1, the axial losses are an inevitable result of using a propeller to generate thrust, while the rotational losses do not contribute to thrust actively. A pre-swirl generator aims, amongst other, to reduce the loss of energy due to rotation in the wake. The concept of pre-rotation will be discussed in the next section.

2.2 Effect of a pre-swirl stator

The main aim of adding pre-swirl, or pre-rotation, is to lower propeller rotational losses. Imagine two propellers in open water, both with the exact same geometry and rotating with the same rotation rate see fig. 2.4.

When the wake field of the second propeller is given a homogeneous distributed rotation over the same axis of rotation as the propeller, the thrust generated by the second propeller will change. The direction of the force vector, acting on the propeller blades, is determined by the angle of inflow at the blade. This angle is a result of the speed of advance of the flow, and the rotation rate of the propeller, see fig. 2.5. In case of the second propeller, the speed of advance has two components, an axial and tangential component, caused by the rotation in the wake (n_w). In the figure, the added wake rotation is in opposite direction of the rotation of the propeller. This way, the tangential velocity relative to the blade is increased.

The angle of attack, α, is defined as the difference between the pitch angle of the blade, β_p and the hydrodynamic pitch angle, β_h. The latter is defined by the inflow velocity

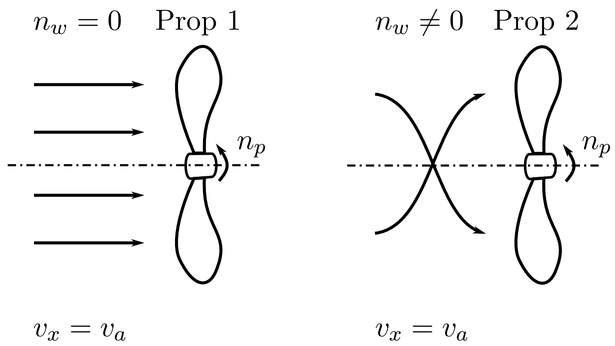

Figure 2.4: Two identical propellers with rotation rate n_p. Propeller 1 in axial inflow conditions, propeller 2 with the same axial inflow and added pre-swirl.

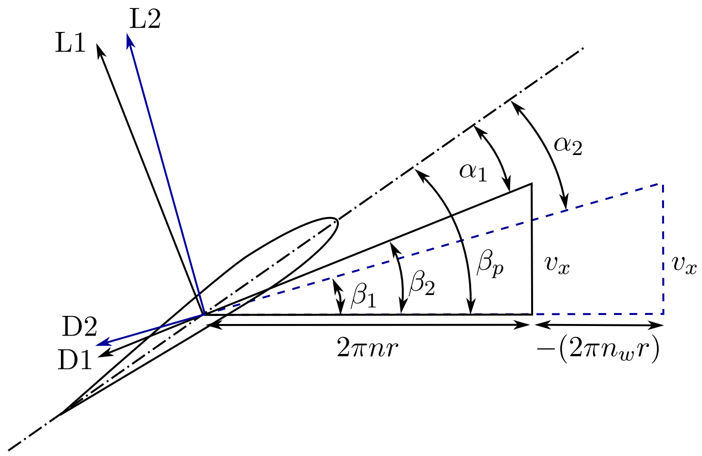

Figure 2.5: Angle of attack without wake rotation (solid line) and with wake rotation (dashed blue line).

and the rotational velocity of the blade.

$$\begin{aligned} \alpha &= \beta_p - \beta_h \\ &= \beta_p - \arctan\left(\frac{V_x}{2\pi nr - V_t}\right) \end{aligned} \tag{2.14}$$

In above equation and figure, the influence of downwash is neglected, although in reality this will introduce a small change in the angle of attack. From eq. (2.14) it can be derived that the change in tangential velocity has the biggest impact for smaller radial distances. Closer to the hub, the apparent velocity of the blade due to its own rotation is smaller compared to a point at the tip of the propeller. Also, when applying pre-rotation in opposite direction of the propeller rotation, this will result in an increase of the angle of attack, while pre-rotation in the same direction of the propeller rotation will result in a decrease of angle of attack. These aspects are important when further designing the pre-swirl stator.

In above example, the rotation rate of the two propellers is kept constant, which leads to an increase of generated thrust when a counter rotating pre-swirl is given to the flow field. An increase in thrust will lead to a higher velocity of the ship, which is not necessary the aim of a pre-swirl stator. For an ESD, the aim is to lower the required energy for travelling at a certain speed. This is accomplished by lowering the propeller rotation rate.

Again imagine the two identical propellers, with the first propeller operating in an purely axial flow field. The second propeller operates in a flow field with a homogeneously distributed rotation, directed in opposite direction of the propeller. Now the second propellers rotation rate is lowered with the same amount as rotation is given to the wake field. In this case, the flow field relative to the propeller is equal to this of the first propeller, resulting in an equal thrust generated by the propeller, see fig. 2.6.

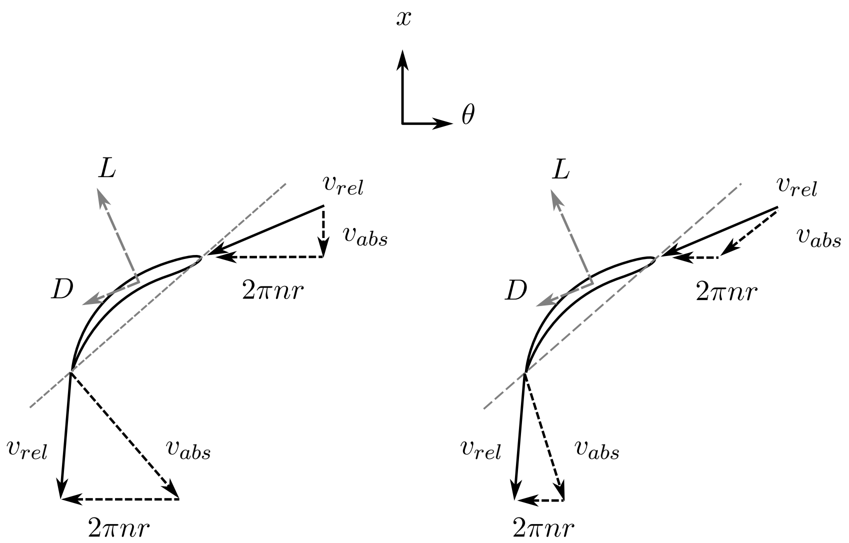

Figure 2.6: Velocity vectors on propeller blade for axial wake field and wake field with pre-rotation.

Looking at the velocity vectors at the trailing edge of the blade, the effect of the lower rotation rate becomes visible. The absolute velocity is changed such that its component in θ-direction has decreased. A reduction of the tangential velocity, will reduce the rotational losses (ROTL)

In order to generate pre-swirl, stator fins are installed in front of the propeller. Addition of these fins will increase the resistance of the hull and hence requires the propeller to generate slightly more thrust. In case the pre-stator is designed at in behind conditions, an asymmetric design should be used in order to change the flow field in an effective way, while reducing the negative thrust (resistance) of the stator [7].

The effect of a pre-swirl stator can be expressed in terms of energy as well. As done for the propeller, the energy equation can be applied to a stator domain. Also the influence of pre-swirl on the propeller can be shown in terms of energy. The next section will elaborate on this.

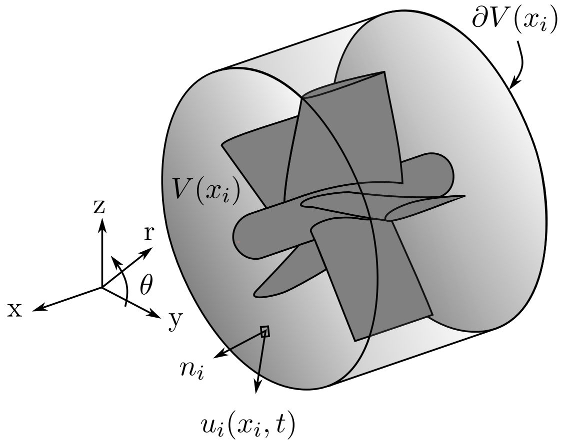

Figure 2.7: Stator control volume.

2.2.1 Energy analysis stator

The energy equation, as described for the propeller, applies for a stator as well. Again, the domain surface can be split in two surfaces; the domain outer surface, ∂V_o, and the stator surface, ∂V_s. As the stator blades are impermeable for the fluid flow and do not rotate, the normal component of the flow velocity equals zero, hence the power flux over the stator blade surface is zero too. This makes sense since the stator cannot perform work while its velocity is equal to zero and when friction is neglected. The stator only changes the direction of the flow, without adding energy. Knowing this, the energy equation for the stator system can be written as depicted in eq. (2.15).

$$\iint_{\partial V_o} \frac{1}{2}\rho||u_i||^2(u_i n_i)dS + \iint_{\partial V_o} p(u_i n_i)dS = 0 \tag{2.15}$$

With a stator creating pre-swirl, the composition of energy fluxes at the aft boundary will differ from the inlet boundary. At the inlet a pure axial energy flux occurs, while part of this axial flux will be transformed into a tangential contribution at the outlet. For the remainder of this analyses, it is assumed that the change in axial velocity due to the induced tangential component is negligible.

The pre-swirl adds rotational kinetic energy to the propeller system. Assuming the induced rotation is homogeneously distributed, like in fig. 2.4, the rotational energy added to the wake field can be defined in terms of wake rotation, n_w.

$$\begin{aligned} E_{kin,rot} &= \frac{1}{2}mv^2 \\ &= \frac{1}{2}m(2\pi n_w r)^2 \end{aligned} \tag{2.16}$$

In order for the propeller to generate a constant thrust, the propeller rotation rate has to change equally with the wake rotation. The propeller power, described in section 2.1.3, corrected for wake rotation reads

$$P_p = 2\pi Q(n - n_w) \tag{2.17}$$

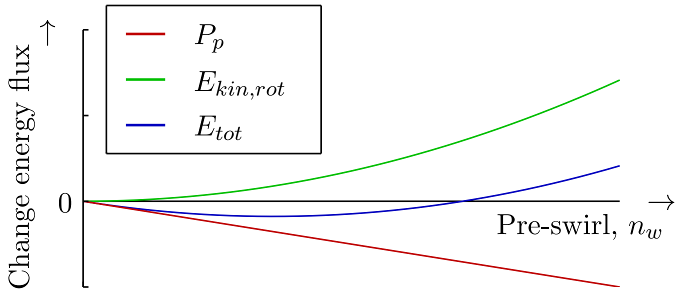

Figure 2.8: Relation between energy flux and wake pre-rotation, plotted for the propeller, the wake rotational kinetic energy and the total energy.

When plotting the change of energy flux of these two equations as a function of the added wake rotation, one can see the potency of pre-swirl, fig. 2.8. For increasing pre-swirl, the propeller power decreases linearly, while on the other hand, the energy added to the system due rotation increases quadratically. The change of the total energy flux is found when the two contributions are summed. This line shows a minimum, which indicates there is an optimal amount of pre-swirl.

2.2.2 Pre-stator efficiency

As noticed before, the conventional definition of propulsive power, (2.4), is not applicable when quantifying the effect of a pre-swirl stator.

This definition only relates the open water efficiency to the interaction of the propeller in behind. To quantify the influence of an ESD, a new efficiency is proposed in [8]. Here, the propeller performance when operating in behind with an ESD is compared to the situation where the propeller is operating without ESD.

$$\begin{aligned} \eta_{esd} &= \frac{n}{n_{esd}} \frac{T_{esd} Q}{T Q_{esd}} \frac{T}{T_{esd}} \\ &= \Delta\eta_{prop} \Delta\eta_{Int} \end{aligned} \tag{2.18}$$

In above equation, the subscript *esd* describes the values for the propeller operating with ESD. The ESD efficiency is split in two parts. The latter, $\Delta\eta_{Int}$, quantifies the interaction of the stator with the ship. If the stator increases the ships resistance, this can be seen as an negative contribution. The first contribution, $\Delta\eta_{prop}$, defines the efficiency change of the propeller, which can be subdivided in a part describing the change in blade loading, and a part describing the blade efficiency.

$$\begin{aligned} \Delta\eta_{prop} &= \frac{n}{n_{esd}} \frac{T_{esd} Q}{T Q_{esd}} \\ &= \Delta\eta_{BL} \Delta\eta_{BE} \end{aligned} \tag{2.19}$$

The change in blade loading efficiency relates the propeller rotation rate without ESD to the rotation rate with ESD. It is a measure of the change in thrust when using an ESD.

In order to keep a constant sailing speed, the rotation rate of the propeller, as depicted in fig. 2.6 has to be reduced. The change in blade efficiency describes the change of the lift vector and radial loading distribution. With this new definition, a better distinction can be made in the different effects of an pre-swirl generator.

Chapter 3

Methods

An overview of the methods used is given in this section. First, the set-up of the optimisation process is presented. This overview will give insight in the programs used in the process and how they interact. From this point, the different methods will be discussed separately and in more detail.

3.1 Optimisation algorithm set-up

The optimisation process consists of four different codes to find an optimal stator geometry, shown in fig. 3.1. The main program, which does the actual optimizing, is Dakota [11]. This optimiser enables a wide range of optimisation techniques and allows the use of other programs to calculate or simulate the responses. In this case, the response is the shaft power needed to drive the propeller, which is to be minimised.

Dakota will perform multiple iterations to find the optimal stator geometry. Each iteration, Dakota starts Propagate, which is a framework developed at Marin to optimise propellers. For this research, parts of Propagate have been changed to be used in the stator optimisation. Propagate controls the simulations and acts as an interface between Dakota and the stator-propeller coupling.

The actual simulation of the pre-swirl stator is controlled in the propeller-stator coupling, or simply coupling. In the coupling, several iterations are performed in which the stator and propeller are separately simulated using Procal, which stand for PROpeller CALculator. Procal is a potential flow code, developed within Marin.

In the next sections, the optimisation process as shown in fig. 3.1 will be discussed bottom up. Explaining the function of each part in more detail.

3.2 Boundary element method simulations

The simulations of both the propeller and stator are performed with Procal (PROpeller CALculator). This code is developed at Marin as part of the CRS collaboration [13]. It is a boundary element method (BEM) which solves an incompressible potential flow

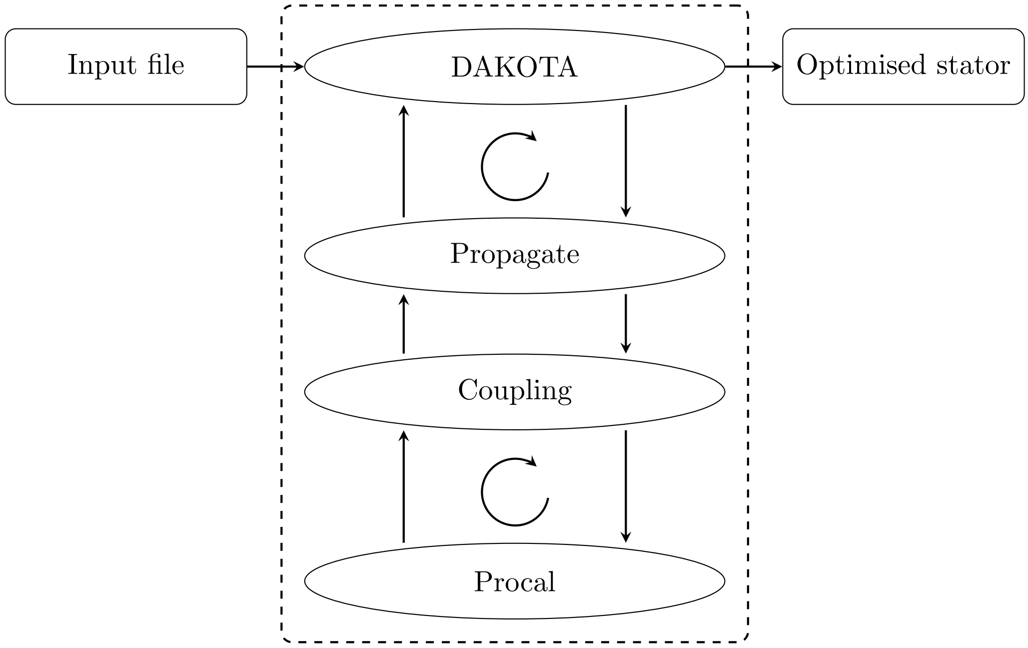

Figure 3.1: Overview of the optimisation algorithm.

around (non-)rotating bodies for both steady and unsteady conditions. Its background will be discussed shortly, starting with the governing equations which are solved by Procal [14].

3.2.1 Governing equations

In potential theory, several assumptions are done to simplify the flow description. With these assumptions, the governing equations for potential flow can be derived from the Navier-Stokes equation.

- No viscous effects, $\mu = 0$;
- No transport or radiation of thermal energy, $\dot{Q} = 0$ and $q_i = 0$;
- Potential flow description: $u_i = \nabla\phi$;
- Irrotational flow, $\omega = \nabla \times u_i = 0$;
- Incompressible flow.

The first two assumptions mainly take out details of the flow description. When simulating a propeller or stator, friction (viscosity) and transport of thermal energy only have a small effect on the flow, whereas neglecting them saves a lot computational effort. With the third assumption, the flow is described as a scalar, instead of as a vector field, reducing the number of equations to be solved. This assumption results in a irrotational flow by definition, the fourth assumption. As the cross product of two gradients equals zero, so does the the cross product of the gradient with the potential flow description, eq. (3.1). The concluding assumption is not necessary to get to a potential flow description, however it is an assumption done in the Procal code.

$$\begin{aligned} \nabla \times \nabla &= 0 \\ \nabla \times u_i &= \nabla \times \nabla\phi \\ &= 0 \end{aligned} \tag{3.1}$$

With these assumptions the continuity equation (conservation of mass) reduces to the Laplace equation, while the momentum equation can be rewritten as the (unsteady) Bernoulli equation.

$$\begin{gathered} \nabla^2\phi = 0 \\ \rho\frac{\partial\phi}{\partial t} + \frac{1}{2}\rho u_i u_i + p + \rho g h = c(t) \end{gathered} \tag{3.2}$$

The advantage of the potential flow description is its linearity. Laplace's equation can be solved as a linear combination of solutions. Above assumptions will result in a less detailed flow description, which limits the applicability of the potential flow description. However, without all the details, calculations to solve a potential flow problem are low on computational costs.

Lift generating bodies. The potential flow equations do not model lift. Lift is defined as the product of density, absolute velocity and circulation (Γ). In potential flow, the latter component is equal to zero by definition.

$$\begin{aligned} L &= \rho|u_i|\Gamma \\ \Gamma &= \oint_S u_i dC \\ &= \int_S (\nabla \times u_i) dS = 0 \end{aligned} \tag{3.3}$$

Circulation can be incorporated allowing the flow to have a discontinuity of the potential over a surface in the computational domain [15]. This wake surface describes an infinitesimal thin layer of vortices, which carry the introduced vortices to the far field, also known as shedded vortices. The velocity potential is discontinues over this surface, the (normal) velocity and hence also pressure are continuous along the wake surface.

Kutta condition. Presence of a wake surface introduces circulation, which value is unknown. In order to solve the system of equations the Kutta condition is enforced. This condition forces the rear stagnation point to move to a defined point, which is on the trailing edge in case of a wing. Without the Kutta condition, the rear stagnation point will appear on an arbitrary point of the body, depicted in fig. 3.2.

$$u_i \cdot n_i = 0 \tag{3.4}$$

While friction causes the flow to leave the trailing edge in a viscous flow, the Kutta condition takes care of this phenomenon when neglecting viscosity. It is a numerical way to incorporate viscosity in a potential flow.

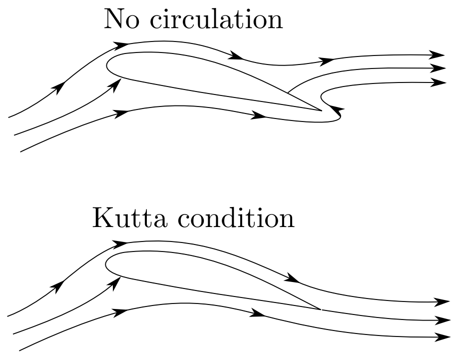

Figure 3.2: Introduction of circulation with Kutta condition.

Viscosity correction. In the post-process, Procal can perform a correction on the results to incorporate viscous effects. The maximum skin friction coefficient is determined and used to include surface roughness in the simulation. The skin friction coefficient, C_f, can be determined with different methods. The Blasius formulation is used for laminar boundary layers, the Bard-Aucher formulation for transition from laminar to a turbulent boundary layer and the Prandtl-Schlichting formulation for turbulent boundary layers.

$$\begin{aligned} \text{Blasius:} \quad & C_f = \frac{1.328}{\sqrt{Re}} \\ \text{Prandtl-Schlichting:} \quad & C_f = \frac{0.044}{Re^{\frac{1}{6}}} - 5.0\frac{1}{Re^{\frac{2}{3}}} \\ \text{Brad-Aucher:} \quad & C_f = \frac{1}{(1.89 + 1.62\log(\frac{\text{chord}}{k_p}))^{2.5}} \end{aligned} \tag{3.5}$$

These relations all use the Reynolds number, Re, which is defined using the chord length as reference length, l_{ref}.

$$Re = \frac{\rho u l_{ref}}{\mu} \tag{3.6}$$

3.2.2 Correction wake rotation

Procal uses the advance coefficient J to determine the actual velocity at the propeller.

$$J = \frac{V_s(1-w)}{nD} \tag{3.7}$$

This definition uses the ship speed V_s, the ships wake fraction w, the propeller rotation rate n and propeller diameter D. When the incoming flow is purely axial, this description is correct. However, in case the wake has an added rotation the inflow velocity at the blade is ill predicted with above expression. In case wake rotation is present, the actual advance coefficient J_{act} corrects the propeller rotation with the rotation in the wake, n_w.

$$J_{act} = \frac{V_s(1-w)}{(n-n_w)D} \tag{3.8}$$

Simulations in Procal can be corrected for wake rotational, by defining the difference in advance coefficient deltaJwake, dJw.

$$\begin{aligned} dJw &= J_{act} - J \\ &= \frac{n_w}{n} J_{act} \end{aligned} \tag{3.9}$$

This facility in Procal is used to correct the advance coefficient in the propeller simulations when coupled to the stator simulations. How this is incorporated in the coupling is discussed in section 3.3.

3.2.3 Grid dependency study

The influence ot the panel distribution can be determined with a grid dependency study. In this research, the uncertainty is determined with the focus on solution verification. With the procedure, described by Eça, Vaz and Hoekstra [16], an interval containing the exact solution with a 95% confidence is created.

$$\phi_i - U_\phi \leq \phi_{exact} \leq \phi_i + U_\phi \tag{3.10}$$

Here U_ϕ is the numerical uncertainty of a certain flow variable, defined as the multiplication of the estimated numerical error with a safety factor. The numerical error can be divided in three components: a round-off- an iterative- and a discretisation error. The discretisation error, ϵ, is defined using a Richardson Extrapolation (RE) and the Grid Convergence Index preferably.

$$\epsilon \simeq \delta_{RE} = \phi_i - \phi_o = \alpha h_i^p \tag{3.11}$$

Where ϕ_i is an integral of a local quantity, ϕ_0 an estimate of the exact solution, while h defines the typical cell size, p is used for the observed order of accuracy and α is an arbitrary constant. Values of ϕ_0, α and p have to be determined in order to estimate the error, this is done using data form at least 4 grids, in the lest squares sense. The order of accuracy is very sensitive for data perturbations, hence the error estimator is reliable using a Richardson extrapolation, only when its convergence is monotonic. Alternative error estimators can be used, assuming the order of accuracy to be $p = 2$.

$$\begin{aligned} \delta_{RE}^{02} &= \phi_i - \phi_o = \alpha_{01} h^2 \\ \delta_{RE}^{12} &= \phi_i - \phi_o = \alpha_{11} h + \alpha_{12} h^2 \end{aligned} \tag{3.12}$$

Both these estimators are determined in a least square sense as well. The error estimator is then changed to a numerical uncertainty using Roache's approach, which uses a safety factor, F_s.

$$\begin{aligned} U_\phi &= F_s|\epsilon| \\ &= 1.25\delta_{RE} + U_s \end{aligned} \tag{3.13}$$

In using this relation, two decisions are of importance: 1) Selecting the most appropriate error estimator and 2) Choosing the safety factor. The second line in above equation gives the uncertainty for a monotonic converging order of accuracy in a range of $0.95 \leq p \leq 2.05$. For other order of accuracy or if no monotonic convergence is found, other relations can be used, as described in [16].

3.3 Stator-Propeller simulations coupling

The coupling acts as an interface between stator and propeller, which are simulated separately. The result from the stator simulation are passed to the propeller simulation and vice-versa, till the coupling converges. Figure 3.3 shows an overview of the coupling procedure. Below, each step in the procedure is discussed.

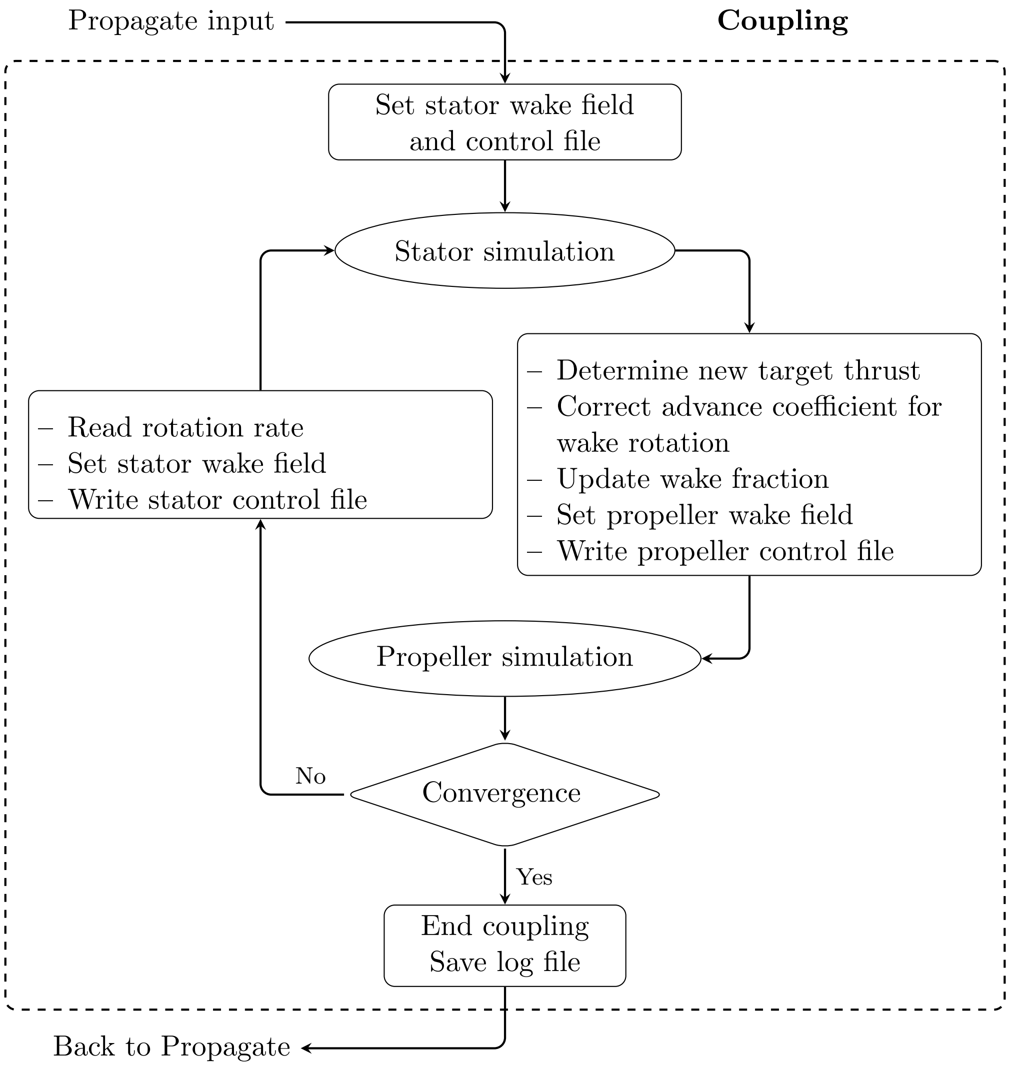

Figure 3.3: Overview of the coupling process.

Input and start. A nominal wake field has to be defined at the start of the coupling. This can be an axial inflow, for example, or a ship wake. The control file needed to run the stator simulation is set with the correct velocity and reference length before the stator simulation is started. In this simulation, the flow around the stator is solved, with an additional output of the wake field at the location of the propeller as depicted in fig. 3.4a. The wake field velocities are determined from the nominal wake, given as input, plus the induced velocities of the stator.

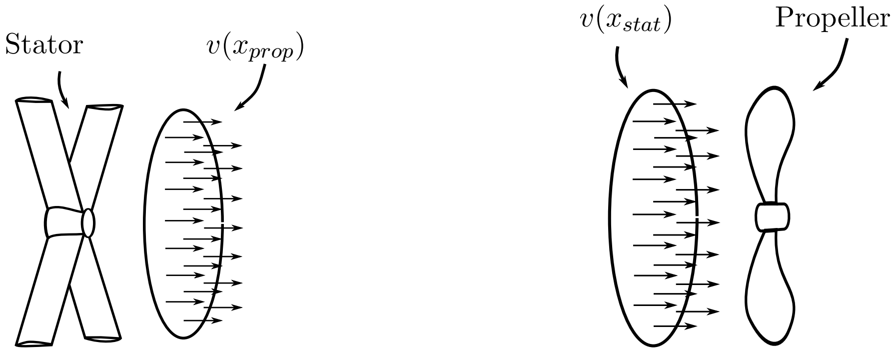

(a) Stator simulation **(b)** Propeller simulation

Figure 3.4: Wake fields calculated during each simulation of both propeller and stator.

Results stator simulation The force and wake field data, obtained from the results, are used to set the propeller simulation control file. The propeller target thrust (T_{prop}) is updated with the stator thrust (T_{stat}) to meet the nett thrust (T_{nett}) needed to reach the ships design speed.

$$T_{prop} = T_{ship} - T_{stator} \tag{3.14}$$

The average wake rotation is determined to update the advance coefficient, as explained in section 3.2. The wake rotation is calculated by integrating the tangential velocity (v_t) from $v(x_{prop})$ over the wake area.

$$n_w = \frac{1}{\pi(r_{tip}^2 - r_{hub}^2)} \int_{r_{hub}}^{r_{tip}} \int_0^{2\pi} \frac{v_t}{\pi r} \frac{V_s}{D} r d\theta dr \tag{3.15}$$

In above equation, the tangential velocity and radius are made dimension full using the ship speed (V_s) and propeller diameter (D) respectively. The radius of the propeller hub and tip are defined by r_{hub} and r_{tip} respectively.

The wake fraction (w) is calculated from the propeller wake field in order to calculate wake rotation correction more accurately. It is defined as the fraction of the difference in the actual speed of advance of the propeller (V_{ad}) with the ship speed (V_s).

$$\begin{aligned} w &= 1 - \frac{V_{ad}}{V_s} \\ V_{ad} &= \frac{1}{\pi(r_{tip}^2 - r_{hub}^2)} \int_{r_{hub}}^{r_{tip}} \int_0^{2\pi} v_x(x_{prop}) r d\theta dr \end{aligned} \tag{3.16}$$

Where $v_x(x_{prop})$ defines the axial velocity of the propeller wake field.

Results propeller simulation. With the adjusted control file and the resulting wake field, the propeller simulation is performed. The propeller simulation solves the flow around the propeller and calculates the wake field at the location of the stator, as depicted in fig. 3.4b. The wake field is defined as the nominal wake plus the propeller induced velocities. This wake field is used as input for the stator in the next iteration. The coupling reads the propeller rotation rate from the solution and stores this to update the propeller rotation rate in the next iteration.

Convergence check. Each iteration, convergence of the results is checked after the propeller simulation. The difference of the stator thrust and average axial velocity at the propeller is calculated.

$$\begin{aligned}\Delta T_{stat} &= \left|\frac{T_{stat}(i-1) - T_{stat}(i)}{T_{stat}(i-1)}\right| \\ \Delta V(x_{prop}) &= \frac{1}{A_{prop}} \iint\limits_{A_{prop}} \left|\frac{v_{x,prop}(i-1) - v_{x,prop}(i)}{v_{x,prop}(i-1)}\right| r dr d\theta\end{aligned} \tag{3.17}$$

Where i denotes the iteration number. The coupling procedure is stopped when both $\Delta T_{stat} < 10^{-4}$ and $\Delta V(x_{prop}) < 10^{-4}$, or after the 6$^{\text{th}}$ iteration. This hard brake is to keep the calculation time limited. A file with coupling process parameters is saved and used to return process data to the optimisation. In section 4.3, the strength of the coupling is tested, here the assumptions of 6 iterations will be discussed as well.

3.4 Matlab interface: Propagate

Propagate serves as an interface between the coupling and the optimisation software. It is a set of Matlab scripts which checks whether or not the entered settings are correct. It collects all parameter files created by Dakota and transforms these files to a sampling plan. The sampling plan contains a parameter for each optimisation variable for all stators in that generation. Using this sample plan, Propagate then creates stator geometries and panel files, and launches a coupling simulation for each stator.

For example, a generation contains 120 stators: Dakota generates 120 parameter files, which are transferred to a sample plan by Propagate. Next, Propagate creates panel files for each stator and launches the coupling 120 times all together.

While the coupling calculations are performed, Propagate waits until all coupling simulations are completed. Propagate reads all the results and creates a response file. This response file is converted into results files which are returned to Dakota.

3.5 Optimisation process

The optimisation process is controlled by the program Dakota [11, 12]. A genetic algorithm is used to search for an optimum in the design space, which is defined by the design parameters, x_n, and their range, with box constraints $[a_n \; b_n]$, eq. (3.18). In this thesis, the optimisation is performed with a single object function, f_i). The aim is to

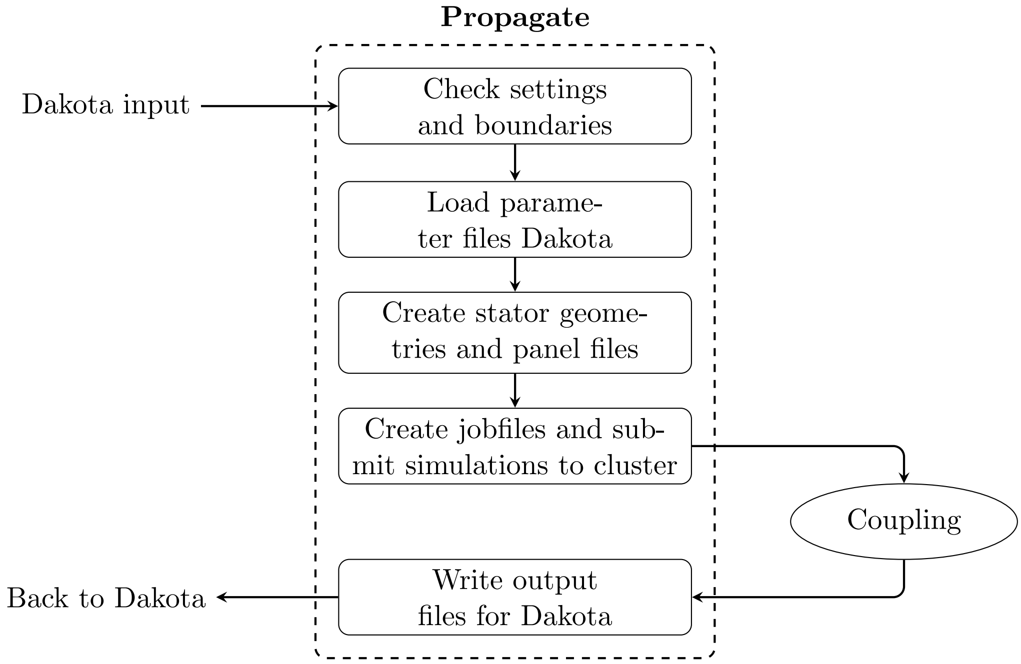

Figure 3.5: Workflow diagram of propagate stator code

minimise the propulsive power, P_p, required to sail the ship at a constant velocity. Each optimisation parameter is given a range, and no (in)equality constraints are given.

$$\begin{aligned} f_i(x_n) &= \min(P_p) \\ x_n &\in [a_n \; b_n] \end{aligned} \tag{3.18}$$

Genetic algorithms are global optimisation methods which allow for optimisation problems to have multiple optima. The algorithm creates a first generation from a set of random numbers. Each new generation is created according to an elitist function: the 10 best 'parents', i.e. the 10 best performing designs, are selected and supplemented with new design points, also know as 'child' designs. The child designs are defined using a two point cross-over technique: the breeding process.

Compared with gradient based optimisations, use of a genetic algorithm comes with higher computational costs. This choice is justified since there is a chance of having multiple optima, while the object function does not have a gradient definition. Also, using a potential flow solver, calculations are relatively cheap, hence the computational costs are still relatively low.

In the Dakota control file, above settings are stored together with the generation size and maximum number of generations. Using Dakota's system interface, a set of parameter files is created each generation, and passed through to propagate. Results are returned with a set of result files from Propagate, which is read by Dakota and evaluated before generating a new generation. This way, simulations can be performed in parallel, which reduces the computational time compared to serial optimisation, where a simulation has to be finished before a new simulation is started.

When a simulation is not converged, this result should be discarded. Dakota has four options to handle these results: abort, retry, recover and continuation. In the first case, the entire optimisation will be stopped, while in the second case the simulation would be resubmitted. Re-submitting the exact same simulation would give the same result, while stopping the entire optimisation is rather rigorous since a non-converging result is not substantially influencing the results. The continuation option would be the preferred option. In that case, a new attempt is made where the optimisation parameters are redefined on a point between the failed 'target' simulation and a nearby 'source' simulation which did converge. With this option however, the optimisation could crash in the first generation, since is there are no 'source' simulations available yet. Therefore the recovery mode is used. In this mode, a not-converged simulation will be given an pre-defined value which is far from the expected optimum. This way, the optimisation is pulled away from failing optimisation points.

At the end of the process, either when the maximum number of generations is reached or when the maximum number of iterations is reached, Dakota ends with returning a file which contains the ten best performing data points. A list of all parameters per population and their results is returned as well.

3.5.1 Design parameters and parametrisation

A pre-swirl stator can be defined using several design parameters, listed in table 3.1. The pitch defines the angle of inflow of the stator blade, the chord determines the width of the blade. Both influence the lift generating capacity of the blades, and hence the pre-swirl that is generated. The thickness influences the drag and strength of a blade, while the chamber is linked to the lift generated by the blade. The x-distance of the stator determines the distance of the stator relative to the propeller. The closer the stator is to the propeller, the more will suction, induced by the propeller, influence the flow over the stator.

Table 3.1: Stator design parameters and possible radial distributions.

Design parameter	Radial distribution	DOF
Pitch	Constant/Linear/Bezier	1/2/6
Chord	Constant/Linear/Bezier	1/2/6
Thickness	Constant/Linear/Bezier	1/2/6
Chamber	Constant/Linear/Bezier	1/2/6
x-distance	Constant	1
Number of blades	Constant	1
Diameter	Constant	1
Blade tangential position	Constant	1

The number of blades influences the resistance of the stator and the distribution of the induced velocity. A higher number of blades will increase the resistance but can create a more homogeneously spread rotation. The stator diameter defines the radial extend of the generated pre-swirl. Though pre-swirl is most effective for smaller radii, this does not necessary mean the stator diameter should be small as well. Vortices can develop at the stator tip, which have a negative effect on the propeller, an effect which should be kept in mind when designing a stator. Finally, the blade tangential position. This determines the position of the blades relative to each other. In open water, an axial symmetric stator would be the most obvious choice in order to generate a homogeneous distributed pre-swirl. For a stator operation in behind, it can be advantageous to design an asymmetric stator to generate a more homogeneous propeller blade loading [8].

Design parametrisation

In order to define the stator geometries, and to be able to vary these geometries, the first four stator design parameters are described with radial distributions. Three different parametrisation definitions are available in the optimisation frame-work, to describe the radial distribution. The first option is a constant distribution over the radius. The second is a linear distribution and the third uses a Bezier curve definition [18].

With the constant distribution, the design parameter is constant over the entire radius and hence it has only one degree of freedom (DOF) to describe the design parameter. With the linear distribution, the design parameter is described with two parameters, being the parameter value at the stator hub 'par hub' and at the stator tip 'par tip', depicted in fig. 3.6. Hence, the linear distribution has two degree of freedom. In case the Bezier distribution is used the number of parameters increases to six degrees of freedom: Ly, Clx, Cly, Crx, Cry and Ry. In the optimisations, a trade off will have

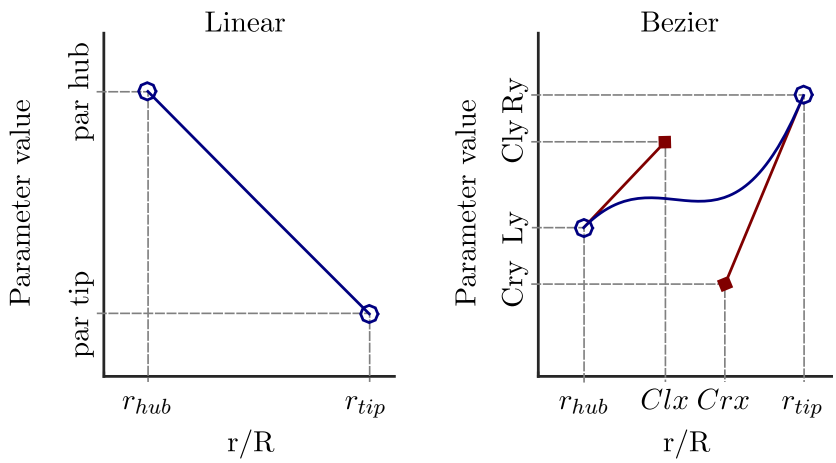

Figure 3.6: Visualisation of linear- and Bezier parametrisation.

to be made between computational effort/time and design details. Use of the Bezier parametrisation will result in a more detailed and possibly better performing stator design, while the increase of degrees of freedom taken into account in the optimisation will increase the computational effort and time of the optimisation.

3.5.2 Design parameter study method

The influence of each design parameter is investigated with a cross-validation method [17]. In this method, all unique and converged results are combined in one data set. A model to predict the response is made for each optimisation parameter, based on the data set. For each model, the RMSE (Root Mean Square Error) is determined and compared with the RMSE of the other models. The optimisation parameter that yields the smallest RMSE on addition to the model, is the parameter with the largest influence on the response and hence, is the design parameter which has the biggest influence on the effect of the pre-swirl stator.

This parameter is added to the model, and above process is repeated for the remaining optimisation parameters, till al parameters are ranked.

3.5.3 Optimisation test cases

In order to test the optimisation frame work, two tests are defined. It was decided to focus on varying three main design parameters: the chord, pitch and camber of the stator blades. In an open water optimisation, five blades will be created with an equal distance relative to the neighbouring blades. The position of the stator relative to the propeller is constant as well and the diameter is equal to the diameter of the propeller.

In the first test case, the three parameters will be defined and varied with a linear distribution. This results in an optimisation with six optimisation variables. Three optimisations will be performed with different generations sizes and number of populations. This way, the most efficient settings can be determined and more insight will be gained in the capabilities of the optimiser.

The second test case, the design parameters will be defined with a Bezier parametrisation. One optimisation will be performed with a population size and number which is based on the knowledge gained from the first optimisation.

Results of these test cases are presented in chapter 5. First, the methods described in this chapter will be tested in order to find the right set-up to use the optimisation interface, this is discussed in chapter 4.

Chapter 4

Method verification

The numerical tools described in previous chapter were tested for convergence and accuracy. This chapter will describe the general settings and the test case used in this research. Also grid dependency studies were performed for both propeller and stator, and the convergence of the coupling procedure was investigated.

4.1 Test Case

The described models were tested using a propeller from the LeanShips project [19]. In this project a conventional propeller design was compared with a large diameter propeller design. The latter propeller was used as a test case in this research. Figure 4.1 shows the geometry of the test case propeller.

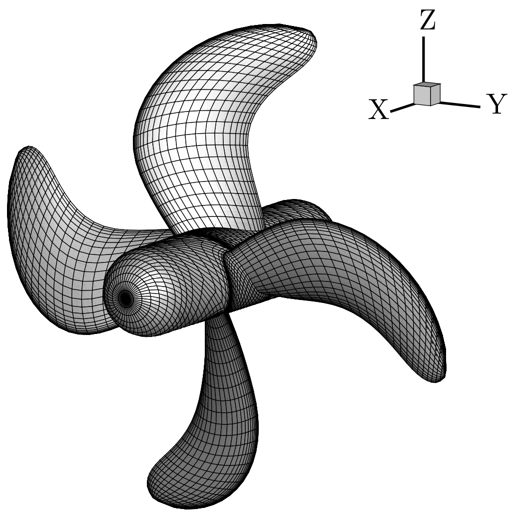

Figure 4.1: Plot of the test case propeller.

The stator optimisation were all performed at the ships design speed, which is 13 knots. Table 4.1 shows an overview of the operational conditions used in the simulations. The operational conditions were derived from the the propeller operating in behind, so the propeller operating in a ships wake field, and transformed to open water operation conditions. The open water conditions, i.e. the propeller operating in a homogeneous axial inflow, were used in all simulations in this research.

Table 4.1: Operational and surrounding conditions used in the test case simulations.

Operational conditions			
Prop diameter	D	7	m
Design speed	V_d	13	kts
Speed in open water	V_s	4.626	m/s
Propeller rotation rate	n	1.083	rps
Advance coefficient	J	0.610	[-]
Thrust	T_{ow}	599.0	kN
Torque	Q_{ow}	620.6	kNm
Power	P_{ow}	4223	kW
Surrounding properties			
Water density	ρ	1025.9	kg/m3
Kinematic viscosity	μ	1.189e-6	m2/s
Atmospheric pressure	p_{atm}	1.025e5	Pa
Gravitational acceleration	g	9.81	m/s2

4.1.1 Flow field without stator

The performance of the propeller in open water was investigated to compare the results in case a pre-swirl stator is installed. In order to do so, the wake field 0.5R aft of the propeller was calculated. In fig. 4.2 the wake fields location, relative to the propeller is depicted. The average wake rotation and kinetic energy fluxes were determined for the wake surface, shown in table 4.2, also the axial energy flux in front of the propeller was determined. The added energy flux by the propeller is given as a percentage of the propeller power as well. In this analysis, work by pressure was neglected, therefore the percentages do not add up to 100%. The energy fluxes are defined by the integral over the wake field surface of the kinetic energy.

$$E_i = \int_0^{2\pi} \int_{r_{hub}}^{r_{tip}} \frac{1}{2}\rho(v_i V_s)^2 \frac{1}{2} V_s D r dr d\theta \tag{4.1}$$

Where the local velocity component (v_i) is made dimension full with the ship velocity (V_s) and the radius (r) is made dimension full with half the diameter ($0.5D$).

The propeller increases the flow velocity and induces rotation, which resulted in higher axial energy fluxes and induced rotation in the wake, which are the rotational losses

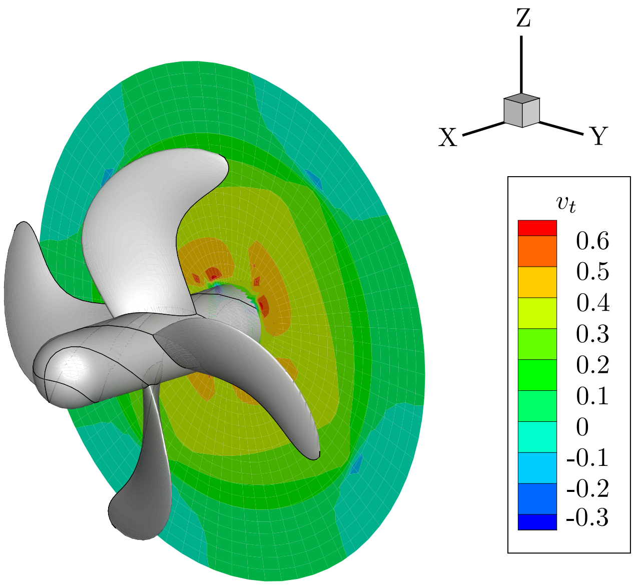

Figure 4.2: Plot of the propeller with wake field contour of the tangential velocity, aft of the propeller at $x/R = -0.5$.

Table 4.2: Comparison of energy fluxes over front and aft wake field section and the difference between the two sections.

		$x/R =$	Inflow	-0.5	% P_{ow}
Average rotation wake	n_w	[rps]	0	0.07	–
Axial kinetic energy flux	E_x	[kW]	2756.7	6278.5	83.4
Tangential kinetic energy flux	E_t	[kW]	0	214.2	5.1
Radial kinetic energy flux	E_r	[kW]	0	14.1	0.3

(ROTL) described in section 2.1.2. To make this visual, the axial and tangential velocity contour behind the propeller are plotted in fig. 4.3. In both contours, the four propeller blades are visual. The difference of the radial energy flux was relative small and ignored in the remaining analysis. Here the velocities are plotted as the local velocity (u_i), made dimensionless with the ship velocity (V_s).

$$v_i = \frac{u_i}{V_s} \tag{4.2}$$

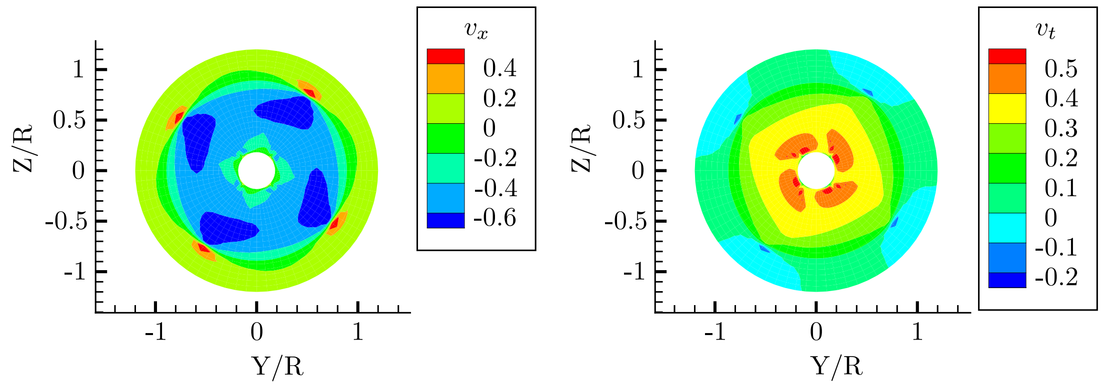

Figure 4.3: Induced axial velocity contour in front and aft of the propeller, normalised with the ship speed.

4.2 Boundary Element Method

In order to find the correct settings, several test were performed with the boundary element method Procal. A grid study for both the propeller and stator have been conducted, which are presented in this section.

4.2.1 Grid dependency study propeller

The LeanShip propeller was simulated with different grid meshes to determine the uncertainty of the results and to find suitable grid settings. The uncertainty verification was done based on the theory as presented in section 3.2.3.

Six geometrical similar grids were created using the gridding guidelines and simulated in open water settings [20]. The main settings for the simulations were based on the settings presented in table 4.1. In table 4.3, the number of panels used for the different grids is presented, where N_c defined the number of panels in chord wise direction, N_r the number of panels in radial direction, N_u the number of panels in upstream direction, N_d the number of panels in downstream direction and N_t the number of panels between the blades. Around the leading- and trailing edges the mesh was refined, as well as at the blade root and tip. The refinement factors used are printed in table 4.4

Table 4.3: Panel distribution over six grids for uncertainty analysis.

	N_c	N_r	N_u	N_d	N_t
G08	8	8	4	4	3
G16	16	16	8	8	6
G24	24	24	12	12	9
G32	32	32	16	16	12
G48	48	48	24	24	18
G64	64	64	32	32	24

Table 4.4: Grid refinement factors propeller.

Area of refinement	Symbol	Value
At leading edge	Sp_{LW}	0.003
At trailing edge	Sp_{TE}	0.15
Towards tip	Sp_{TP}	0.015
Towards hub	Sp_{HB}	0.05

In fig. 4.4, the results of the uncertainty analyses are shown for the thrust coefficient K_t, the torque coefficient K_q and the propeller efficiency η_p. The figures show the uncertainty percentage U and the accuracy of the fit, p. In table 4.5, the uncertainty percentages are printed for each grid, except the one but finest grid.

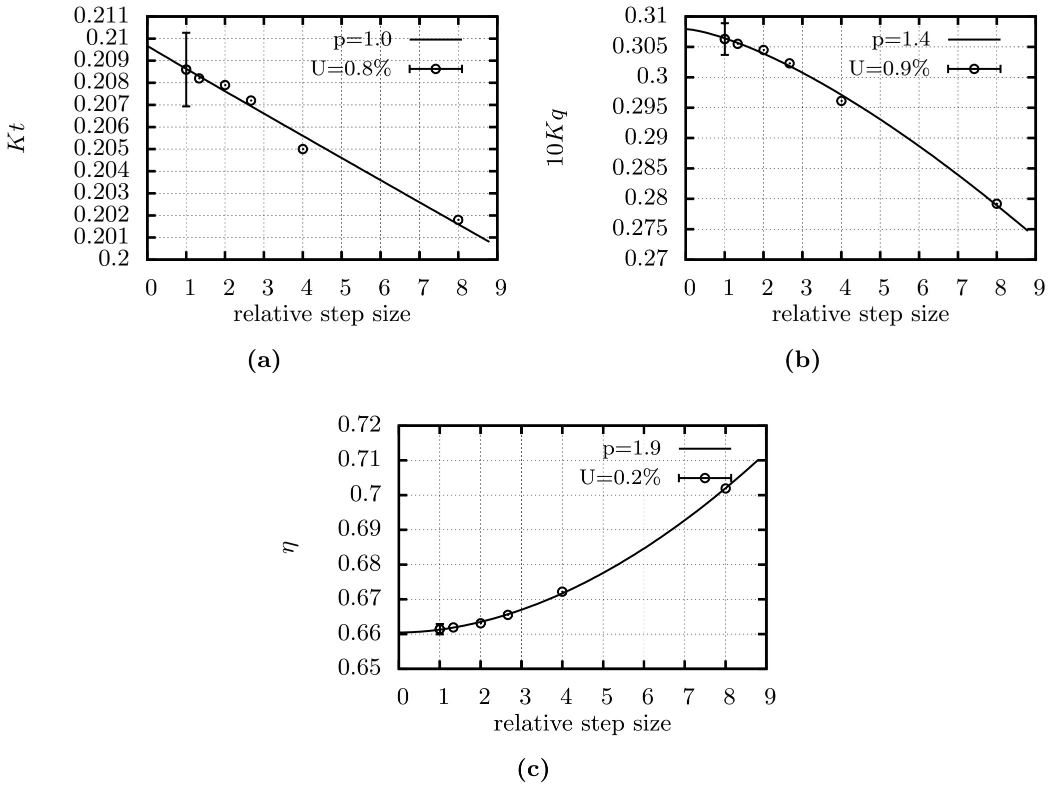

Figure 4.4: Uncertainty percentages and polynomial fit for the thrust coefficient, the torque coefficient and the propeller efficiency simulated with six different grids.

The uncertainty was determined from a well fitted curve for each of the three result parameters and a low uncertainty percentage for each of the parameters was found. For G24 and finer, all uncertainty percentages are below 5%, and keeping in mind the calculation time, it was decided to use the grid settings from G24 for the simulations done in this research. The geometry shown in fig. 4.1 shows a grid with the settings from G24.

Table 4.5: Numerical uncertainty percentage of the thrust coefficient, torque coefficient and the uncertainty. In the last column, the calculation time is printed.

	$U_\phi(K_t)$ [%]	$U_\phi(K_q)$ [%]	$U_\phi(\eta_p)$ [%]	Time [mm:ss]
G08	5.3	13.3	7.5	00:01.56
G16	2.9	5.1	2.2	00:01.56
G24	1.9	2.9	1.1	00:06.32
G32	1.5	2.1	0.7	00:14.37
G48	-	-	-	01:40.45
G64	0.8	0.9	0.2	06:00.41

4.2.2 Grid dependency study stator

A grid dependency study was performed for the stator as well. The stator used for this study had four blades with a cross-section based on a NACA-4412 airfoil All design parameters were kept constant over the radius, the pitch of the blades was 8° in order to have a significant lift effect of the blades. The uncertainty study was done as presented in section 4.2.

The study was performed with six geometrical similar grids with an increasing number of grid points. A first grid was created according to the gridding guidelines [20], depicted in fig. 4.5. Based on this grid, one coarser and four finer grids were developed. In table 4.6, the number of panels used for the different grids is presented, where N_c defines the number of panels in chord wise direction, N_r the number of panels in radial direction, N_u the number of panels in upstream direction, N_d the number of panels in downstream direction and N_t the number of panels between the blades. Around the leading- and trailing edges the mesh was refined, the same was done at the blade root and tip. The refinement factors used are printed in table 4.7

Table 4.6: Number of panels on each component for the six different stator grids.

	N_c	N_r	N_u	N_d	N_t
SG15	15	12	6	6	3
SG20	20	16	8	8	4
SG30	30	24	12	12	6
SG40	40	32	16	16	8
SG50	50	40	20	20	10
SG60	60	48	24	24	12

The uncertainty was determined for the thrust- and torque coefficient, see fig. 4.6. In table 4.8 an overview is given of the uncertainty percentage and the simulation time for each grid. For grid SG50 it was not possible to determine the uncertainty using the calculation tool available at Marin. In case of a more detailed uncertainty study, this problem should be solved. For this study, the results as listed in fig. 4.6 have been used.

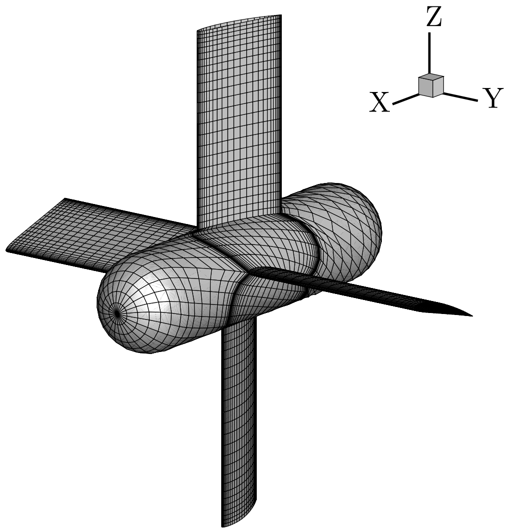

Figure 4.5: Mesh grid20 of the stator geometry, the blade cross-sections were based on a NACA-4412 profile.

Table 4.7: Grid refinement factors stator.

Area of refinement	Symbol	Value
At leading edge	Sp_{LW}	0.003
At trailing edge	Sp_{TE}	0.003
Towards tip	Sp_{TP}	0.015
Towards hub	Sp_{HB}	0.03

From grid SG40 and finer, the computation time increased rapidly, without changing the accuracy much. The grid SG30 had a low simulation time, while the uncertainty of both the thrust- and the torque coefficient were well below 5% which is considered to be low enough to perform the stator simulations.

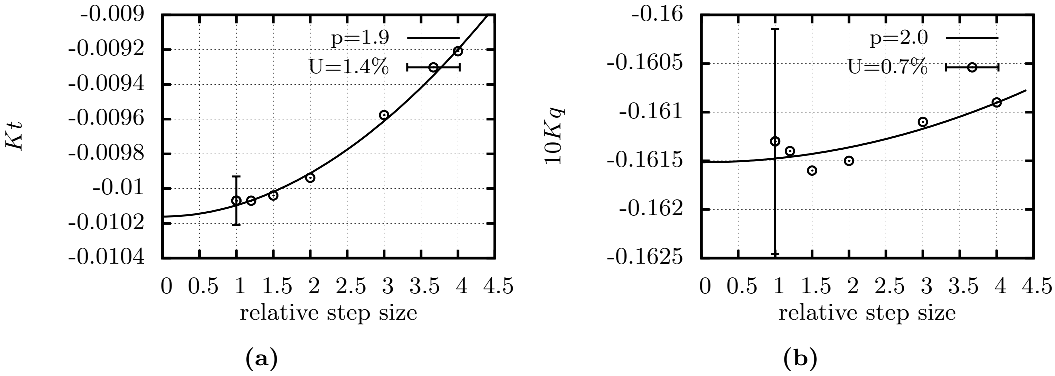

Figure 4.6: Uncertainty percentages and polynomial fit for the thrust coefficient and the torque coefficient of stator, simulated with six different grids.

Table 4.8: K_T and K_Q uncertainty and computation time of stator grid study for each grid.

	$U_\phi(K_t)$ [%]	$U_\phi(K_q)$ [%]	Time [mm:ss]
SG15	13.5	1.5	00:03.50
SG20	7.9	1.1	00:09.36
SG30	3.7	0.9	00:42.72
SG40	2.3	0.8	01:52.10
SG50	-	-	03:33.72
SG60	1.4	0.7	08:58.12

4.3 Coupling iteration convergence

The convergence of the iteration differences was evaluated to check the assumed iteration criterion to be used. As explained in section 3.3, the two criterion used are the difference between current iteration and previous iteration of stator thrust and the average axial wake velocity provided at the propeller. The difference in stator thrust (ΔT_{stat}) was compared with the L_{inf}-norm of the pressure coefficient (Cp_{stat}) on the stator and the iteration difference of the propulsive power (ΔP). The second criterion was compared with the L_{inf}-norm of the axial wake velocity at the location of the propeller ($v(x_{prop})$) and with the iteration difference of the propulsive power.

In fig. 4.7, the stator geometry used in the iteration convergence study is depicted together with the propeller. This stator was tested among three other designs, all with different geometries. The results were comparable for each of the design tested, hence the iteration differences are printed for this simulation only.

In fig. 4.8, the results of this test are printed. The iteration differences roughly decreased logarithmic for increasing iteration. For the wake velocities and the propulsive power, the difference between iterations became too small to be measured. For the force and pressure on the stator this was after the seventh iteration. This showed that the interaction between the two simulations is relative weak. Based on these results it was decided to truncate the simulations if the iterations differences are smaller than 10^{-4}, or after the sixth generation. In the latter case, the results are labelled as not-converged and hence they will be considered as a bad solution in the optimisation.

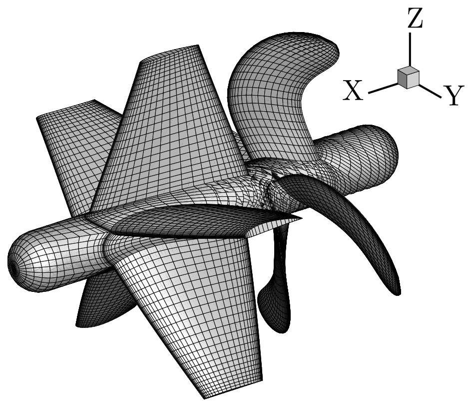

Figure 4.7: Stator and propeller geometry used in the iteration convergence study.

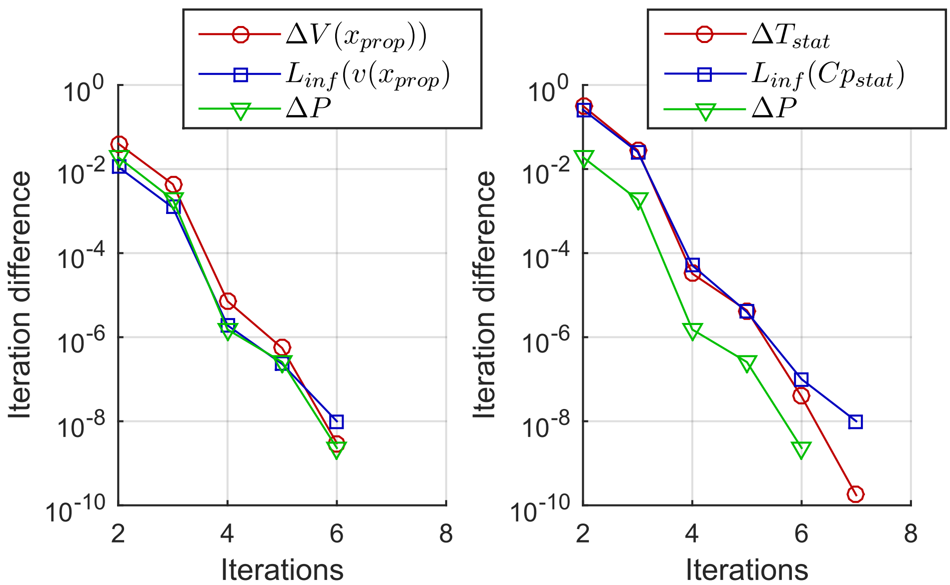

Figure 4.8: Iteration differences over the number of iterations performed in the stator-propeller coupling simulation.

Chapter 5

Results and discussion

As explained in section 3.5.3, the optimisation routine was tested with two different cases. In the first test case, three design variables were given a linear parametrisation distribution and varied in the optimisation. This resulted in an optimisation with 6 optimisation variables. The test case is denoted with DV6. In the second tests case two design parameters were given a Bezier parametrisation and varied in the optimisation. This gave the optimisation 12 variables and this test case is denoted with DV12. The results of these cases are both discussed in four steps.

First the optimisation results are presented, showing how the optimisation algorithm evolved from the first to the last generation. Secondly, the best performing design and its parameters will be compared to the chosen design space. Next, the influence of the optimisation parameters is analysed, before examining the actual performance of the best stator design. To end the analysis, an efficiency and energy analysis was performed based on the theory explained in section 2.2.

After discussing the two optimisation cases, a hydrodynamic analysis of the best performing stator designs of the two optimisations are compared with the propeller without stator. Here, the forces and pressure on the propeller and stator blades are discussed.

To conclude this chapter, the results from the BEM simulations of the pre-swirl stator are compared with results from a RANS simulation.

5.1 First optimisation test case

For this test case, a linear parametrisation was used to describe three stator design parameters; the stator chord, pitch and camber. This lead to an optimisation with six optimisation parameters. With these design parameters, three optimisations where performed, each with a different population size. The first optimisation started with a population size of 80 iterations (P80), the second had 120 iterations (P120) and the last optimisation 160 iterations (P160).

The test case propeller, presented in section 4.1, is used in the optimisation process for open water, as discussed in section 3.5.3.

5.1.1 Evolution first test case

In fig. 5.1 the resulting power of each simulated stator is plotted over the population number it was part of. This is done for each of the three optimisations. The blue triangles depict P80, the green P120 and the red P160.

Each of the three optimisations converged to a minimum response of 3998 kW, which is a reduction of 5.3% compared to the power of a propeller without stator. In the first population, the spreading of optimisation parameters within the design space resulted in a wide response range. This range of the response decreases rapidly over the next population in each of the three optimisations. From the fifth population onwards, the maximum response in a population differed less than 0.5% of the final minimum response for both the P80 and P120 optimisation. For the P160 this difference was obtained from the fourth population onwards.

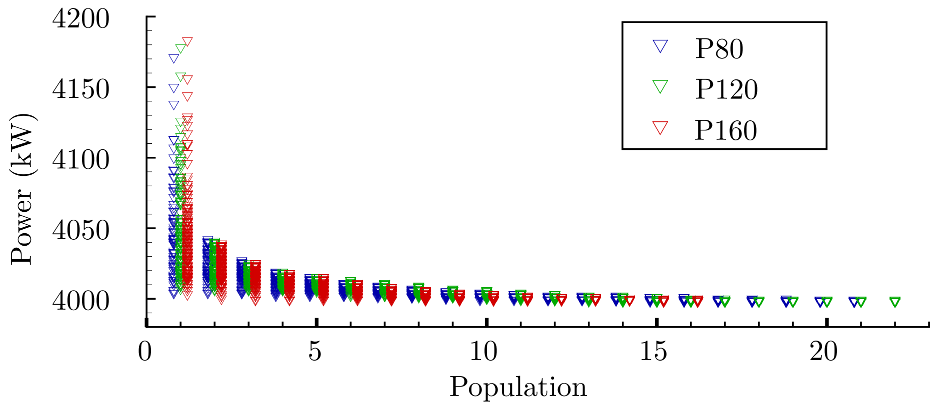

Figure 5.1: Development of the predicted power for each iteration plotted over the number of generations.

The minimum response in a population approached the final minimum with a difference of less then 0.1% in population seven (P80), eight (P120) and two (P160). This showed that the P160 optimisation is relative faster to find an optimal solution compared to the P80 and P120 optimisations. This is reflected in the total number of populations as well. The P160 optimisation ended after the 16th population, while the P80 and P120 needed 21 and 22 populations to finish the process respectively.

Regarding the computational effort, the total number of iterations used in each of the optimisation is listed in table 5.1. In this table, the number of unique iterations is shown also. The P80 and P120 used 42% of unique iterations compared to 47% in the P160 optimisation. This suggests the P160 optimisation searched a relative wider range of parameter values within the design space then the other two optimisations, which would increase the certainty of finding the global optimum.

Calculation time of the optimisations was not tracked, however, can be estimated from the maximum calculation time for one coupling simulation. A coupling simulation will take 2 hours at maximum. The time needed to launch all coupling simulations in a population and to process the results was in the order of minutes. Assuming the time

Table 5.1: DV6 population sizes, and resulting numbers for the three optimisations.

	P80	P120	P160
Population size	80	120	160
Populations	21	22	16
Total iterations	1680	2640	2560
Unique iterations (#)	701	1112	1205
Unique iterations (%)	42%	42%	47%

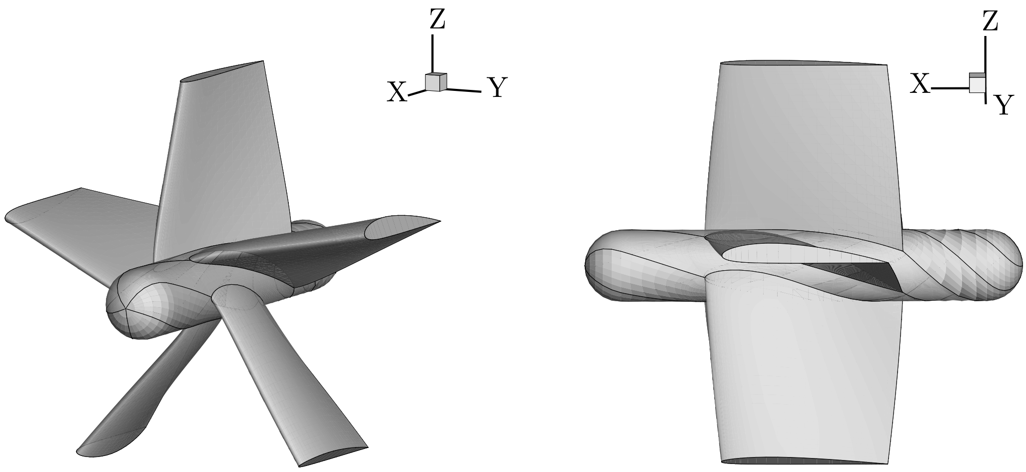

Figure 5.2: Best performing geometry in P80 optimisation

to compute one population took 2 hours, the P80 would have taken 42 hours, the P120 44 hours and the P160 32 hours.

As listed in table 5.1, the P160 optimisation used at least five generations less to determine an optimal result, however it used almost double the amount of iterations compared to the P80 optimisation. In case the costs of calculation are negligible compared to time, population size P160 would have lowest costs, while P80 would serve better in case cost of a single calculation is of more importance compared to calculation time.

5.1.2 Comparison best geometries

Each of the optimisations resulted in a 'winner', i.e. a best performing stator geometry, which will be presented next. In fig. 5.3 the radial distributions, defining the shape of the stator geometries, are plotted for each design parameter. For both the chord- and pitch distribution, the resulting distributions were almost equal. The resulting camber distribution showed differences between the different optimisations.

In fig. 5.2, the best performing stator geometry of P80 was printed. The differences between parameter distributions were to small to see much difference between the best performing geometries of P120 and P160, hence only the P80 geometry was depicted.

As can be seen in fig. 5.3, each of the three design parameters was larger at the hub,

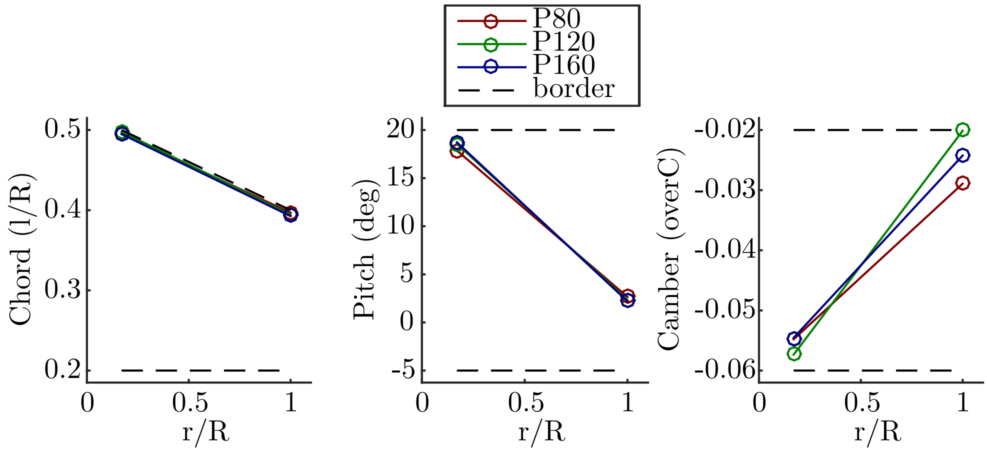

Figure 5.3: Radial distributions of the three stator design parameters for the best performing design from P80, P120 and P160. The distribution is a linear distribution based on the parameter values at the hub and at the tip.

compared to the tip. The chord distribution optimum appeared to be right on the optimisation border, which was not the case for the pitch and camber. The pitch distribution is close to the upper boarder at the hub, and decreased for increasing radius. The camber decreased over increasing radius, and was close to the border on both hub and tip point. Especially the P120 optimisation was close to the upper border at the hub and at the lower border at the tip.

Optimisation parameters which converge to a value close to, or equal to, the border value can indicate that the design space is too small and that a global optimum exists outside the design space. In the current optimisation, this could be the case for the chord settings, however a further increase of the stator chord is not feasible since the space available in front of the propeller is in general limited.

5.1.3 Parameter study

To get a better insight in the different parameter values of the best performing stator geometries, a parameter analysis was performed. The influence of each optimisation parameter was tested using the cross-validation method described in section 3.5. In fig. 5.4, the error of the response model with respect to the response data is plotted as a function of the optimisation parameter added to the system. The optimisation parameters are listed in decreasing order of importance, which differs for the three optimisations.

In each of the three optimisations, the pitch has the greatest influence on the response model. Addition of pitch at the hub to the model caused a reduction of the error by approximately 0.2% for each optimisation, and addition of pitch at the tip further reduced the error with approximately 0.1%. This behaviour was similar for each of the three optimisations, which means that in all cases the pitch hub parameter had the largest influence on the optimisation results, followed by the pitch hub parameter.

For the remaining parameters, the chord and camber both at the hub and tip, the order of importance was different for the three optimisations. The influence of these parameters

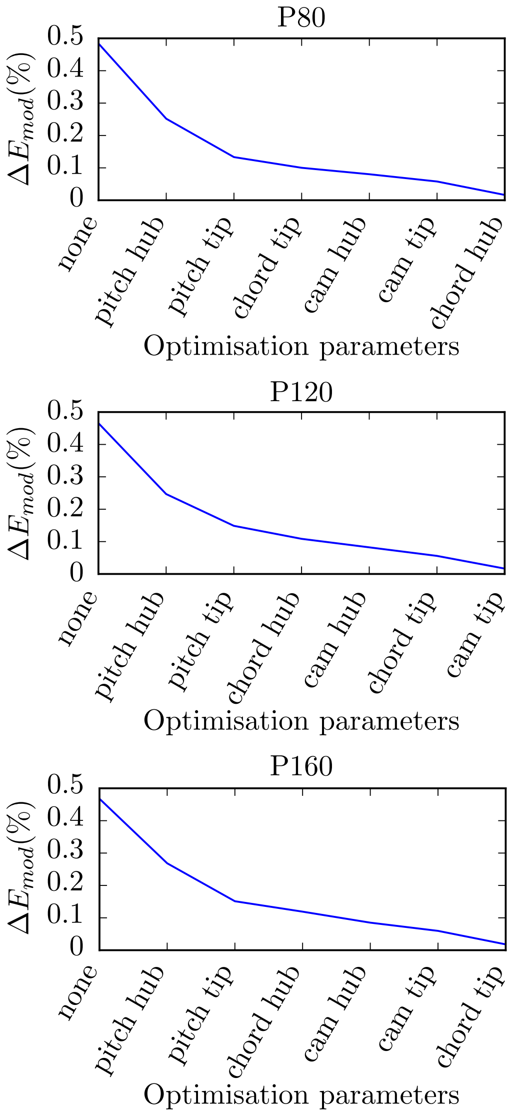

Figure 5.4: Error between model and optimisation response data for decreasing influence of the optimisation parameter. Error difference printed in %

was relative small compared to the pitch hub and pitch tip. Addition of these parameters all resulted in a reduction of approximately 0.03%, compared to a difference of 0.2% and 0.1% due to the pitch hub and pitch tip respectively.

The results of above parameter test were partly reflected in fig. 5.5. In this figure, all six optimisation parameters are plotted separately, showing the parameter values for each iteration in the 16 populations in the P160 optimisation. The colour scale represents the response data and the black diamond shows the setting of the best design according to the optimisation routine.

With increasing population number, the chord and pitch parameters all had an increasing preference for a certain value. The main difference between the pitch and chord optimisation parameter was that the pitch starts to shift towards the optimal value immediately from the first geometry onwards, while the chord parameters started to converge after the fifth population. The settings for the camber did not show any real convergence. Settings were spread over more then half of the domain in the last population.

The observed behaviour of the two pitch parameters and the chord at the hub endorse the results of the cross-validation parameter analysis. However, the influence of the chord at the tip would be larger compared to the chord parameters from above reasoning.

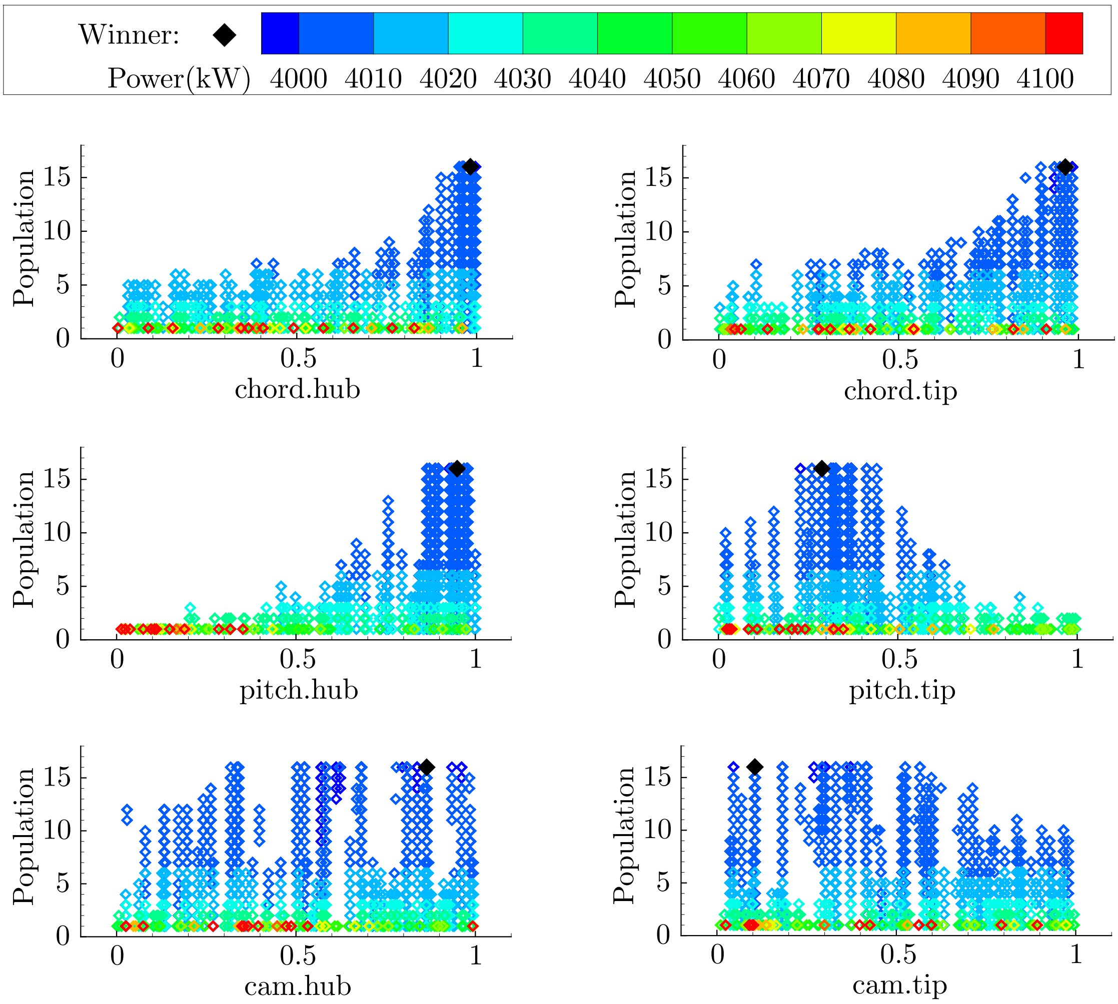

Figure 5.5: Distribution of optimisation parameter values over all generations of the P160 optimisation.

5.1.4 Efficiency and energy analysis P160 winner

The change in performance due to the pre-swirl stator is determined using the efficiency definition presented in section 2.2.2. In this section an expression was introduced to quantify the effect of an ESD. Below, the definition of the stator efficiency, eq. (2.18) and eq. (2.19), is combined.

$$\begin{aligned}\eta_{esd} &= \frac{n}{n_{esd}} \frac{T_{esd}Q}{TQ_{esd}} \frac{T}{T_{esd}} \\ &= \Delta\eta_{BL}\Delta\eta_{BE}\Delta\eta_{Int}\end{aligned} \tag{5.1}$$

In table 5.2, the propeller rotation rate, thrust, torque and power are printed for both the propeller without stator (PNS) and propeller with stator (PWS). From these values, the stator efficiency was determined and added to the table. The PNS parameters were obtained from table 4.1.

Table 5.2: Ship specifications and operational conditions

PNS			
Propeller rotation rate	n	1.083	rps
Thrust	T	599.0	kN
Torque	Q	620.6	kNm
Power	P	4223	kW
PWS			
Propeller rotation rate	n_{esd}	0.999	rps
Thrust	T_{esd}	632.0	kN
Torque	Q_{esd}	636.9	kNm
Power	P_{esd}	3998	kW
Stator efficiency			
Stator efficiency	η_{esd}	1.057	[-]
Change blade loading	$\Delta\eta_{BL}$	1.084	[-]
Change blade efficiency	$\Delta\eta_{BE}$	1.029	[-]
Change interaction	$\Delta\eta_{Int}$	0.948	[-]

Due to the stator, the propulsive efficiency increased with 5.7%. The change in blade loading efficiency ($\Delta\eta_{BL}$), i.e. the reduction in rotation rate of the propeller, was the largest improvement. It was increased by 8.4%. Second, the blade efficiency ($\Delta\eta_{BE}$) was improved by 2.9%. With stator, the propeller generated a higher trust and the torque increased as well. However, the increase in torque was lower compared to the increase in thrust, so the propeller blade had become more efficient. Last, the interaction efficiency caused the stator efficiency to decrease. In open water, the stator generates a negative thrust force, which has to be overcome by the propeller to maintain the design speed. Therefore, the thrust generated by the propeller with stator has to be higher compared to the case without propeller. With stator the interaction efficiency reduced with 5.2%.

Energy analysis

With a pre-swirl stator, the propeller is operating more efficiently. The energy analysis, as performed for the test case without stator, was repeated for the propeller with the

P160 best performing stator. In table 5.3, the energy fluxes and wake rotation are listed for the propeller without stator and with stator. Also the energy fluxes and wake rotation behind the stator, without the influence of the propeller, was determined and listed in table 5.3. In the second part of this table, the percentages of the energy fluxes with respect to the power of the propeller without stator are listed. The energy fluxes were corrected for the energy flux contained in the nominal wake field, which only has an axial energy flux: $E_{x(inflow)} = 2756.7\text{kW}$.

The stator adds a rotation in opposite direction of the propeller and hence converts axial kinetic energy into tangential kinetic energy. The average wake rotation behind the propeller for PWS is reduced with almost 66% compared to the PNS propeller. The tangential kinetic energy left in the wake behind the propeller is decreased from 214.2 kW for the PNS to 28.3 kW for the PWS. This is the reduction of the rotational losses (ROTL) as explained in section 2.2.1.

Table 5.3: Comparison of average wake rotation and energy fluxes in the wake field behind stator and propeller, compared to propeller without stator. The results are given as dimension full value, and as percentage of flux change with respect to the PNS propeller power.

			PWS		PNS
		$x/R =$	0	-0.5	-0.5
Average rotation wake	n_w	[rps]	-0.064	0.021	0.07
Axial kinetic energy flux	E_x	[kW]	2636.2	6303.3	6278.5
Tangential kinetic energy flux	E_t	[kW]	108.8	28.3	214.2
Radial kinetic energy flux	E_r	[kW]	15.1	40.6	14.1
Energy flux as percentage PNS power					
Axial kinetic energy flux	E_x	%	-2.85	83.98	83.40
Tangential kinetic energy flux	E_t	%	2.58	0.67	5.07
Radial kinetic energy flux	E_r	%	0.36	0.96	0.33

In fig. 5.6, contour plots of the tangential velocity (v_t) at the wake fields as discussed above are depicted. The wake rotation due to the stator is located close to the hub mainly. The difference between rotation close to the hub, compared to the tip region can be explained from the stator geometry. At the hub, the blade pitch angle is 18°, while at the tip the pitch angle is 2°. The lift force, and hence the induced rotation depends on the blade pitch angle. For a larger pitch angle, the lift force will increase, as does the induced wake rotation. With a pitch angle around zero, the lift on the stator blade is small, as is the resulting wake rotation.

The effect of wake rotation can be seen comparing the two wake field contours at x/R = -0.5. In case of the PWS, the tangential velocity is relative low and homogeneous distributed, compared to the PNS case. For the latter flow field, the propeller induces a rotation in the wake, mainly close to the hub. This is visualises the difference in tangential kinetic energy fluxes listed in table 5.3. Without stator, the rotational velocity is considerably higher compared to the case with stator.

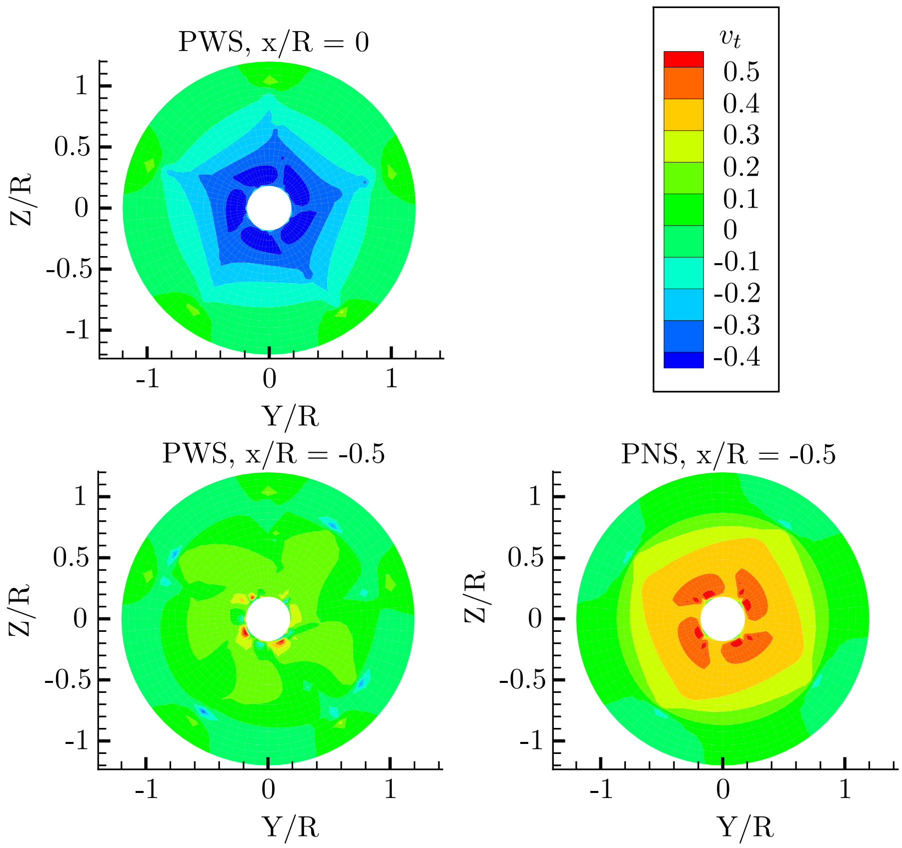

Figure 5.6: Wake field tangential velocity contours at x/R = 0 and x/R = -0.5 for PWS and PNS case. Simulations PWS were performed with best performing stator from the P160 optimisation.

5.2 Second optimisation test case

For the second optimisation case, a Bezier parametrisation was used to describe two design parameters; the chord and pitch. Since the camber had relative little influence, and to reduce the number of optimisation parameters which should improve the interpretation of the results. This way, the process contained twelve optimisation parameters.

The optimisation was performed with a population size of 240 stators over a maximum of 30 generations. In the remaining of this chapter, the results of this optimisation will be indicated as the DV12 optimisation. The results are discussed in the same order as the DV6 optimisation, where in the hydrodynamic analysis the results of the best performing geometry from the DV12 is compared to the best performing stator from P160.

5.2.1 Evolution second test case

The response of each simulation is plotted in fig. 5.7 for each population. In the final population, a response power of 3950 kW was obtained by the best performing geometry, which is an improvement of 6.5% compared with the propeller power without stator.

The response range, i.e. the difference between maximum and minimum response, decreases rapidly after the initialisation. Difference between maximum and minimum response is less then 1% after the third iteration. However, the minimum response keeps decreasing and it is not clear whether or not the optimisation is finished in the 30^{th} population. The general tendency is that the further reduction of the response will be small, as the minimum response only reduced from 3954 kW in the 24^{th} population to 3950 kW in the 30^{th} population. It was decided to analyse to use this result for further analysis. In order to make sure the optimum is reached it is recommended to repeat the optimisation with an higher amount of populations.

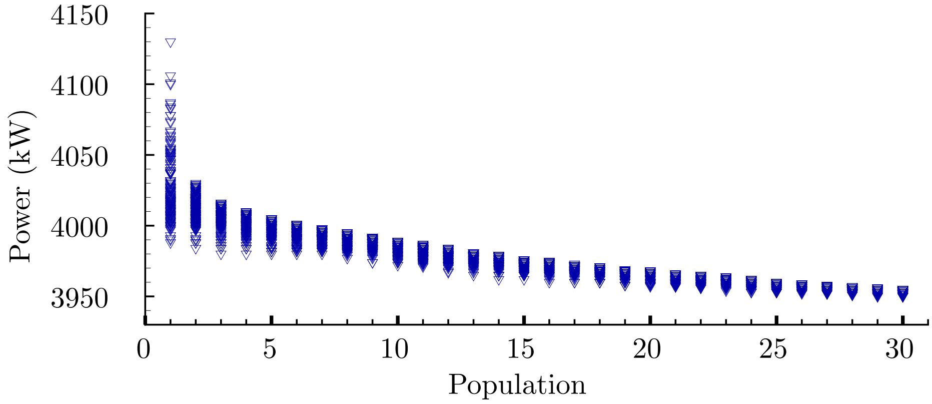

Figure 5.7: Development of the predicted power for each iteration plotted over the number of generations.

In the DV12 optimisation, only one optimisation was performed, instead of three like in the DV6 case. From the evolution as depicted in fig. 5.7 it appears the population size is to small to cover a sufficiently large set of different stator geometries. This could delay the development of the optimisation, which results in a larger number of populations before the optimisation converges. On the other hand, the complexity of the optimisation increased considerably with twice as much optimisation parameters compared to the DV6 case, which will increase the computational time and effort.

The total number of iterations evaluated in the optimisation was 7200, while the number of unique iterations was 2969, which is 41% of the total number of iterations. This is comparable to the P80 and P120 optimisation performed in the DV6 case (table 5.1). In section 5.1.1, it is suggested that for a larger population size, the search space increased, leading to a higher percentage of unique iterations and possibly to a higher certainty of the found optimum being the real optimum in the design range. More optimisations with different population sizes and number of optimisation would be helpful to get a better insight in the optimisation behaviour.

5.2.2 Inspection best geometry

The best performing geometry of the DV12 optimisation is depicted in fig. 5.8. Compared to the geometry from P80, fig. 5.2, the shape of this is more complex, which is enabled by the Bezier parametrisation.

In fig. 5.9, the radial distribution of both the chord and pitch are plotted, together

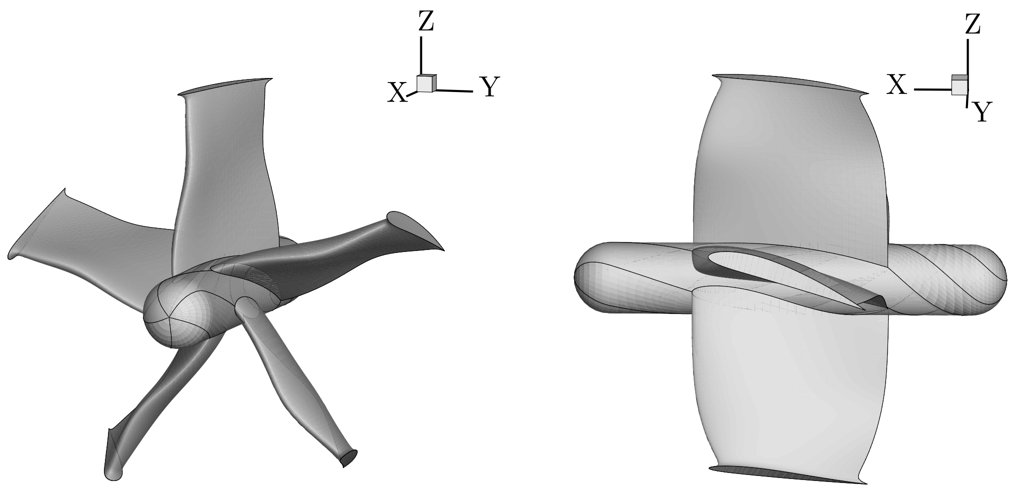

Figure 5.8: Picture of the best performing geometry in DV12 optimisation.

with the boundaries defined by the design space of the optimisation parameters, applied in the DV12 optimisation. For the chord, the begin and end point of the distribution are positioned right at the upper border. It is the right control point which draws the distribution away from the border. This control point causes a steep dip in the chord of the stator, close to the tip, which creates sharp points in up- and downstream direction. From a manufacturing perspective, these points increase the complexity of the geometry, making it more costly to produce the stator. And also, their contribution to the pre-swirl generating capabilities are presumably small.

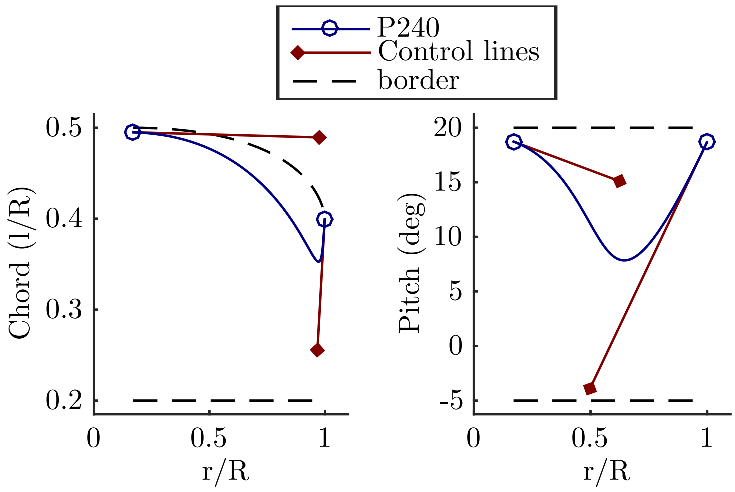

Figure 5.9: Radial distributions of the two stator design parameters, the chord and pitch, plotted for the best performing design in the DV12 optimisation. The distributions are based on a Bezier parametrisation.

The pitch distribution shows that both hub and tip points are located close to the upper border, like in the chord distribution. Here, a decrease between hub and tip is present as well, although less sharp compared to the chord distribution. The increase of the pitch towards the tip is surprising. A larger pitch angle should increase the lift on the blade and hence the generation of pre-swirl. As shown in section 2.2, pre-swirl is more effective close to the hub compared to the tip region. The effect of high pitch at the tip of the stator will be discussed later in the hydrodynamical analysis, section 5.3. First, the influence of the optimisation parameters is discussed.

5.2.3 Parameter study

A parameter analysis as described in section 3.5 is performed for the DV12 case. To recap the meaning of the different parametrisation names, see fig. 5.10 taken form mentioned section.

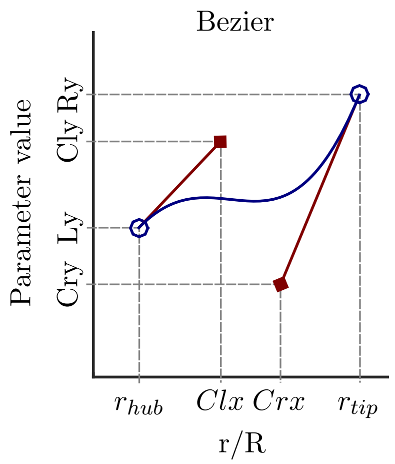

Figure 5.10: Visualisation of Bezier parametrisation.

Figure 5.11 shows that the influence of chord Ly is largest, causing a decrease of the error with 0.2%. The second most influential optimisation parameter is pitch Ry, followed by the pitch at the hub (pitch Ly) with a change of the error with 0.08 and 0.05% respectively. A 'mid-section' is formed by the pitch Cly, the pitch Cry, the chord Ry and chord Cly, for which the error difference is smaller, but noticeable still. The error difference for the remaining five parameters is negligible compared to the other parameters.

What catches the eye is that the chord at the hub has the greatest influence, while in the DV6 optimisation this was the pitch at the hub. In the DV12 optimisation the pitch at the hub comes second so still it has to be seen as an important parameter. Also the pitch at the tip is one of the more influential parameters, which corresponds with the DV6 optimisations.

In the mid-section, the parameters with small influence are all describing the actual value of the parameter, compared to the parameters with negligible influence, which are parameters influencing the radial position of the control points all but one.

An overview of the parameter values of each stator calculated in the optimisation is plotted for each population in fig. 5.12 and fig. 5.13. In the first figure, the optimisation parameters describing the chord are depicted, while in the second figure the pitch parameter are depicted. From the chord parameters, the Ly and Ry converge to a small range relative quickly after the 10^{th} population. The Clx, Cly and Crx also converge to a relative small range, though the preference becomes visible slightly later in the process compared to the Ly and Ry parameters.

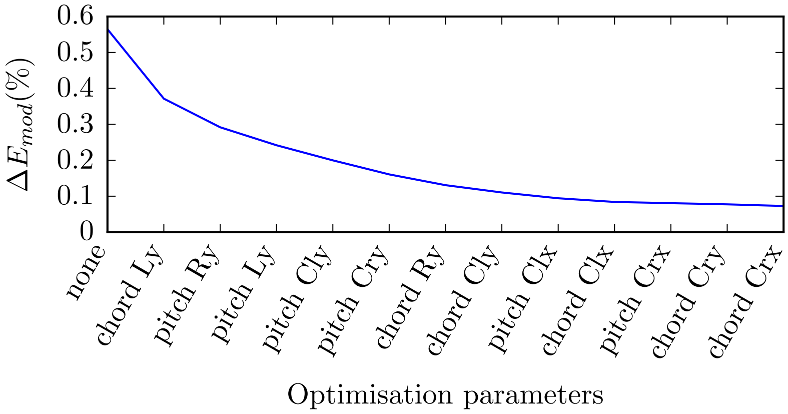

Figure 5.11: Error between model and optimisation response data for decreasing influence of the optimisation parameter. Error difference printed in %

As the reader might have noticed, interpretation of figures like fig. 5.12 and fig. 5.13 is rather subjective. This becomes even more clear with increasing number of optimisation parameters. The parameter study as depicted in fig. 5.11 appears to be more valuable, though results are a bit unexpected for this optimisation.

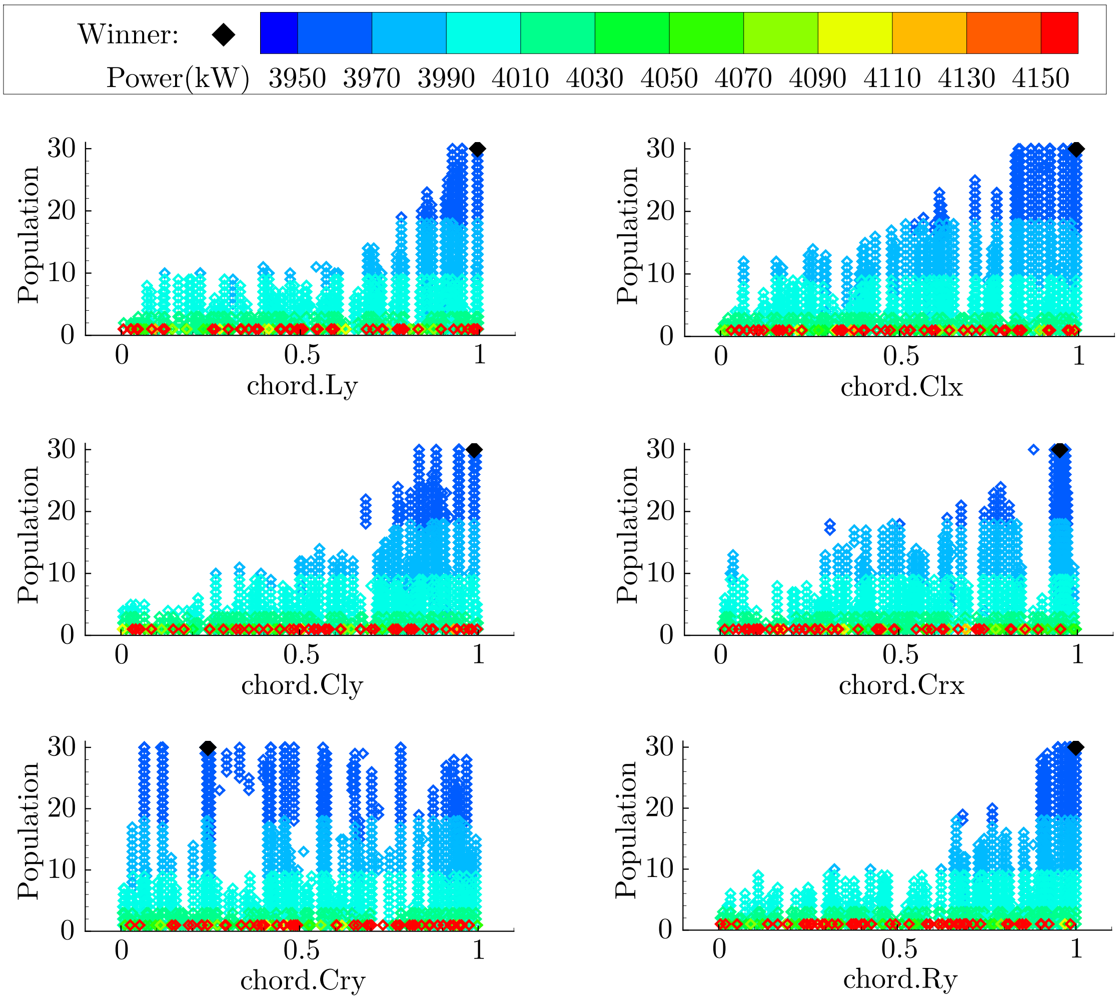

Figure 5.12: Development of the predicted power for each iteration plotted over the number of generations.

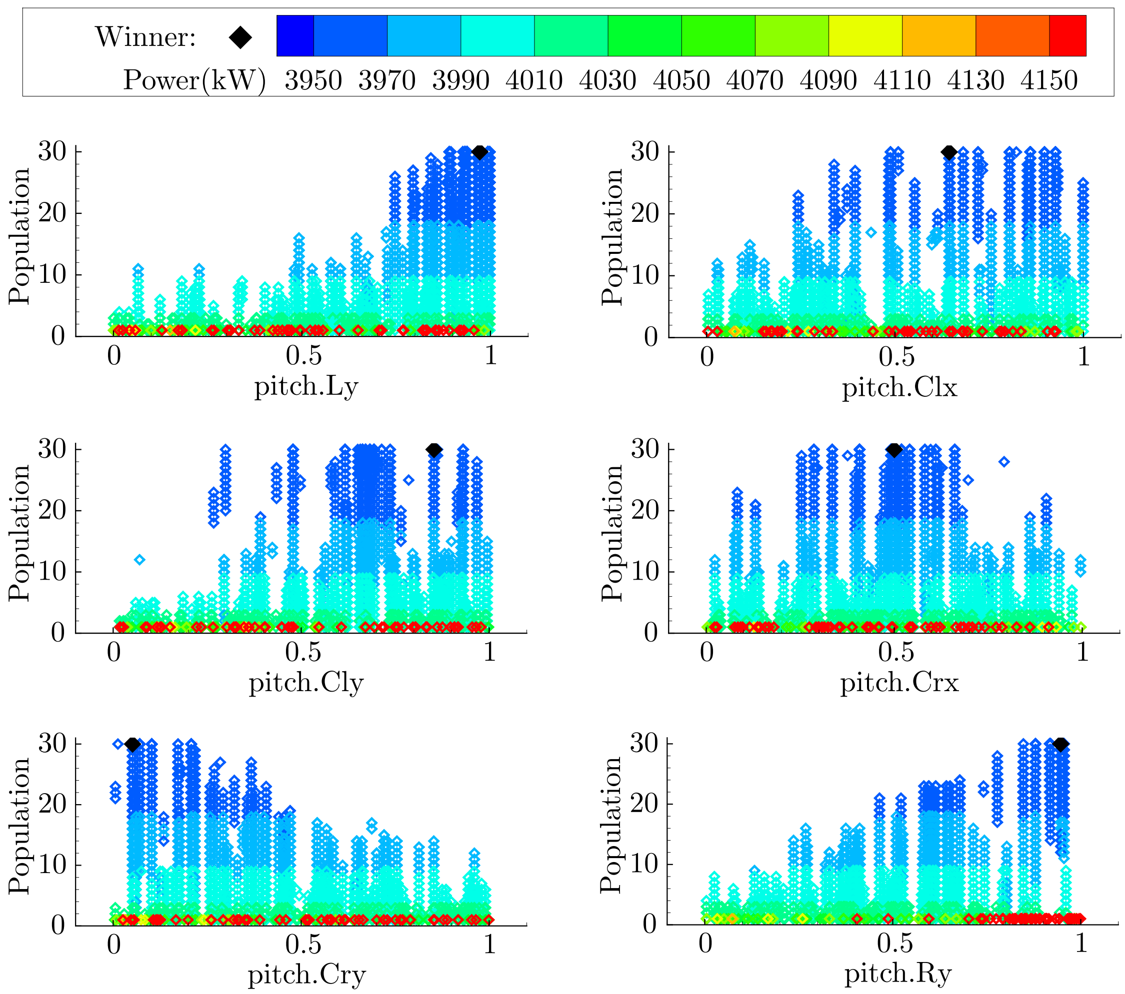

Figure 5.13: Development of the predicted power for each iteration plotted over the number of generations.

5.2.4 Efficiency and energy analysis DV12 winner

Using the definition of ESD efficiency, eq. (2.18), the performance of the best performing pre-stator is determined. In table 5.4, the propeller rotation rate, thrust, torque and power are listed for both the propeller without stator (PNS) and the propeller with stator (PWS). With these values the stator efficiency is determined, and listed in the same table.

Table 5.4: Ship specifications and operational conditions

PNS			
Propeller rotation rate	n	1.083	rps
Thrust	T	599.0	kN
Torque	Q	620.6	kNm
Power	P	4223	kW
PWS			
Propeller rotation rate	n_{esd}	0.985	rps
Thrust	T_{esd}	635.1	kN
Torque	Q_{esd}	638.2	kNm
Power	P_{esd}	3950	kW
Stator efficiency			
Stator efficiency	η_{esd}	1.068	[-]
Change blade loading	$\Delta\eta_{BL}$	1.099	[-]
Change blade efficiency	$\Delta\eta_{BE}$	1.031	[-]
Change interaction	$\Delta\eta_{Int}$	0.943	[-]

With pre-swirl stator, the propulsive efficiency of the stator increases with 6.8%. The blade loading increases in particular, gaining 9.9% efficiency. Also the blade efficiency is increased with stator; the blade efficiency gained 3.1%. Due to the added resistance, the interaction efficiency was reduced by 5.7%. The latter two changes in efficiency are comparable to the change in efficiency as found for the best performing geometry in the P160 optimisation, section 5.1.4, while the change in blade loading is considerably higher.

Energy analysis

Table 5.5 lists the average wake rotation and energy fluxes in the wake behind the propeller for the PWS and PNS simulation. For the PWS, the energy fluxes were determined behind the stator at the location of the propeller, but without the influence of the propeller. In the second part of table 5.5, the percentages of the energy fluxes with respect to the power of the propeller without stator are listed. The energy fluxes are corrected for the energy flux contained in the nominal wake field, which only has an axial energy flux: $E_{x(inflow)} = 2756.7\text{kW}$.

The stator induced a rotation in the wake, in opposite direction of the propeller rotation,

Table 5.5: Comparison of average wake rotation and energy fluxes in the wake field behind stator and propeller, compared to propeller without stator. The results are given as dimension full value, and as percentage of flux change with respect to the PNS propeller power.

			PWS		PNS
		$x/R =$	0	-0.5	-0.5
Average rotation wake	n_w	[rps]	-0.070	0.016	0.07
Axial kinetic energy flux	E_x	[kW]	2567.0	6169.7	6278.5
Tangential kinetic energy flux	E_t	[kW]	127.2	29.9	214.2
Radial kinetic energy flux	E_r	[kW]	20.6	50.6	14.1
Energy flux as percentage PNS power					
Axial kinetic energy flux	E_x	%	-4.49	80.82	83.40
Tangential kinetic energy flux	E_t	%	3.01	0.71	5.07
Radial kinetic energy flux	E_r	%	0.49	1.20	0.33

with an average rotation of 0.07 rps. This results in an average wake rotation of 0.016 rps behind the propeller, which is a reduction of 77.9% relative to the wake rotation behind the propeller without pre-stator. This is reflected in the tangential kinetic energy flux which is present behind the propeller. Without stator, the tangential energy flux behind the propeller is 214.2kW which is 5.07% of the PNS power input. With stator, this flux is 29.9kW, which is 0.71% of the summed energy fluxes, a reduction of 4.36% compared to the PWS simulation.

In fig. 5.14, the difference in wake rotation is visualised. This figure shows contour plots of the tangential velocity for the wake fields listed in table 5.5. In the upper left part of the figure, the pre-swirl generated by the stator is depicted. Close to the hub, the amount of pre-swirl is higher compared to the tip region. Even though the stator has a considerable pitch and chord at the tip, the tangential velocity in the wake is relative low. The induced pre-swirl cancels out the rotation of the wake behind the propeller which becomes clear comparing the lower two contours. Apart from some small spikes, the tangential velocity for the PWS is relative low, while for the PNS clear regions with rotation around the hub.

The contour plot of the PNS show some spikes with both high and low velocities. These spikes might be a result of the large pitch at the tip of the blade, causing a relative large pressure difference and hence a higher velocity locally.

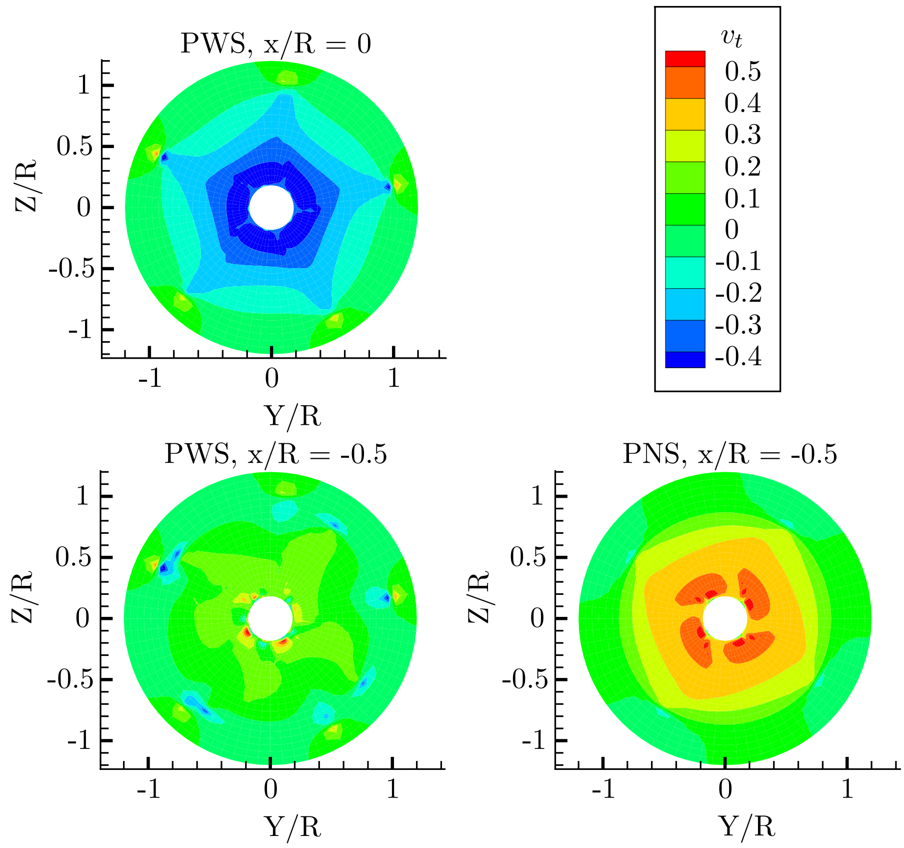

Figure 5.14: Wake field tangential velocity contours at x/R = 0 and x/R = -0.5 for PWS and x/R = -0.5 PNS case. Simulations PWS were performed with best performing stator from the P240 optimisation.

5.3 Hydrodynamic analysis of the best stators

The flow around the propeller and stator is further investigated in order to get a better insight in the effect of the stator. Results of simulation with the two best performing stator geometries from the P160 and DV12 optimisations are compared with the result of the simulation of the propeller without stator.

5.3.1 Propeller hydrodynamics

Figure 5.15 depicts the axial- and tangential forces on the propeller blade and their fraction: the blade efficiency. These forces are made dimensionless with the density, a reference velocity and a reference length. The later two being the ship velocity and propeller diameter in this case.

$$
\begin{aligned}
F_x &= \frac{F_x(r)}{\rho V_{ref}^2 L_{ref}^2} \\
F_t &= \frac{M_x(r)}{r \rho V_{ref}^2 L_{ref}^2}
\end{aligned}
\tag{5.2}
$$

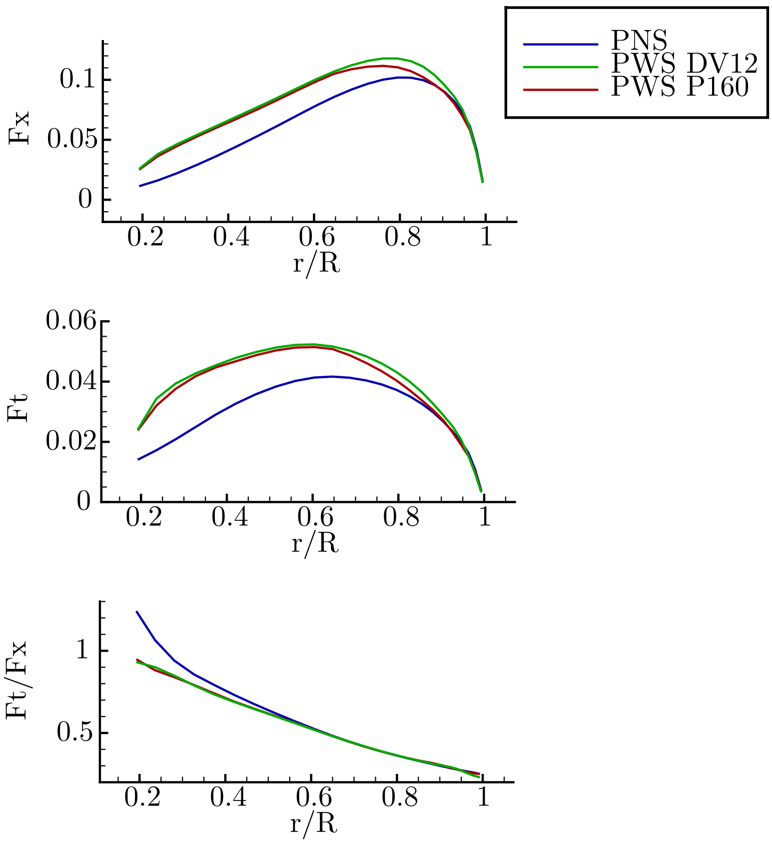

Figure 5.15: Comparison of the axial and tangential forces and blade efficiency acting on the propeller blade operating in open water without stator (PNS) and with stator (PWS) from both the DV12 and P160 optimisation.

The first two graphs show an increase of both the axial and tangential force for the PWS simulations over almost the entire radius, from the hub up to approximately 0.85 r/R. This increase for PWS compared to PNS corresponds with the increase in thrust and torque listed in table 5.3 and table 5.5.

The blade efficiency is influenced by the stator as well, though not in the same extend as the forces. From the hub, up to half the radius, the blade efficiency is improved. Which shows that close to the hub, the increase of the tangential force was relative lower compared to the increase in axial force when a pre-swirl stator was added to the simulation. In the PWS DV12 simulation, the forces were slightly higher, relative to the PWS P160 simulation. This could be a result of the larger pitch angle at the tip of the DV12 stator compared to the pitch at the tip of the P160 stator. In terms of blade efficiency, the two stator simulations performed equally.

In fig. 5.16, the forces on the propeller blade are defined normal and tangential to the blade nose-tail line. The normal force, C_n, is higher for the lower radial sections, in case a pre-swirl stator is applied. In contrast, the tangential force, C_t, is lower near the hub given the presence of a stator. The tangential force is positive from nose to tail, hence a negative value will add to the thrust and lower the torque of the blade, which improves the blade efficiency of the propeller.

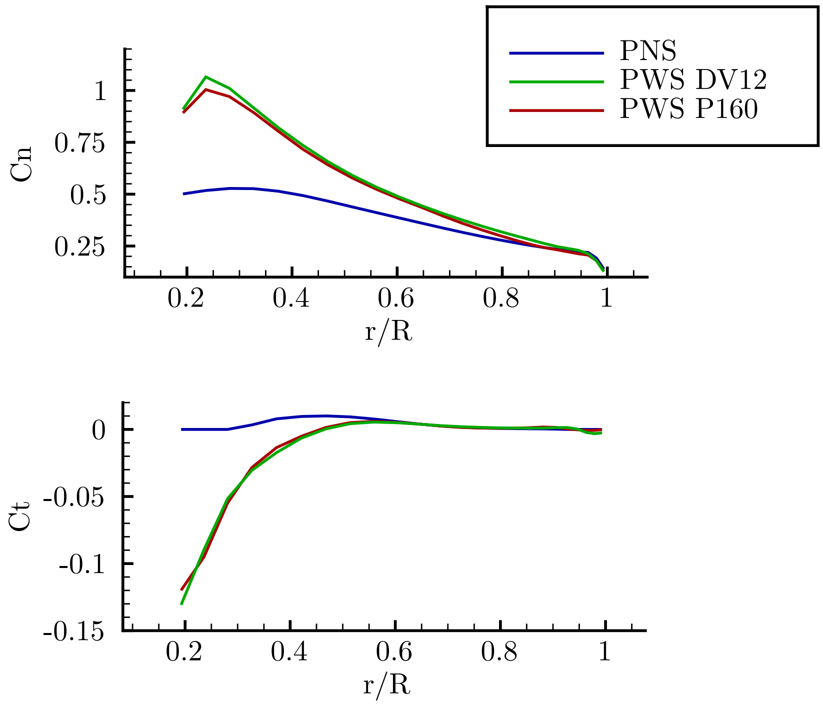

Figure 5.16: Comparison of the sectional normal and sectional tangential forces and blade efficiency acting on the propeller blade operating in open water without stator (PNS) and with stator (PWS) from both the DV12 and P160 optimisation.

The tangential force is nearly equal for the DV12 and P160 stator, while the normal force shows small differences. The greatest difference can be seen close to the hub, where the DV12 stator has a slightly larger value. Also towards the tip, an increase of the force can be seen for the DV12, though the difference is smaller compared to the hub. The increase in normal force is probably due to the higher amount of pre-swirl generated by the DV12 stator. The small difference at the tip could be te result of the pitch being higher at the tip of the DV12 stator.

An overview of the pressure distribution in chord wise direction is given at four radial stations in fig. 5.17. On the lower radial stations, r/R = 0.2 and r/R = 0.4, the pressure lines of the propeller without stator cross around x/c = 0.1. With stator, this effect is reduced; at r/R = 0.4, the pressure does not cross at all, while at r/R = 0.2 the position of the crossing is moved closer to the leading edge. This indicates a considerable shift in the angle of attack due to the pre-swirl. Also the difference between the pressure lines changes favourable, increasing the area between the lines. This corresponds to the increased forces acting on the propeller blade when a pre-swirl stator is added.

Changes in pressure were only present at lower radial stations, which corresponds with the introduced tangential velocity by the stator. The optimisations converged to a solution which added wake rotation close to the hub mainly, as depicted in fig. 5.6 and fig. 5.14. This corresponds with the theoretical concept of pre-swirl explained in section 2.2, that the effect of pre-swirl is the largest when added for lower radial stations.

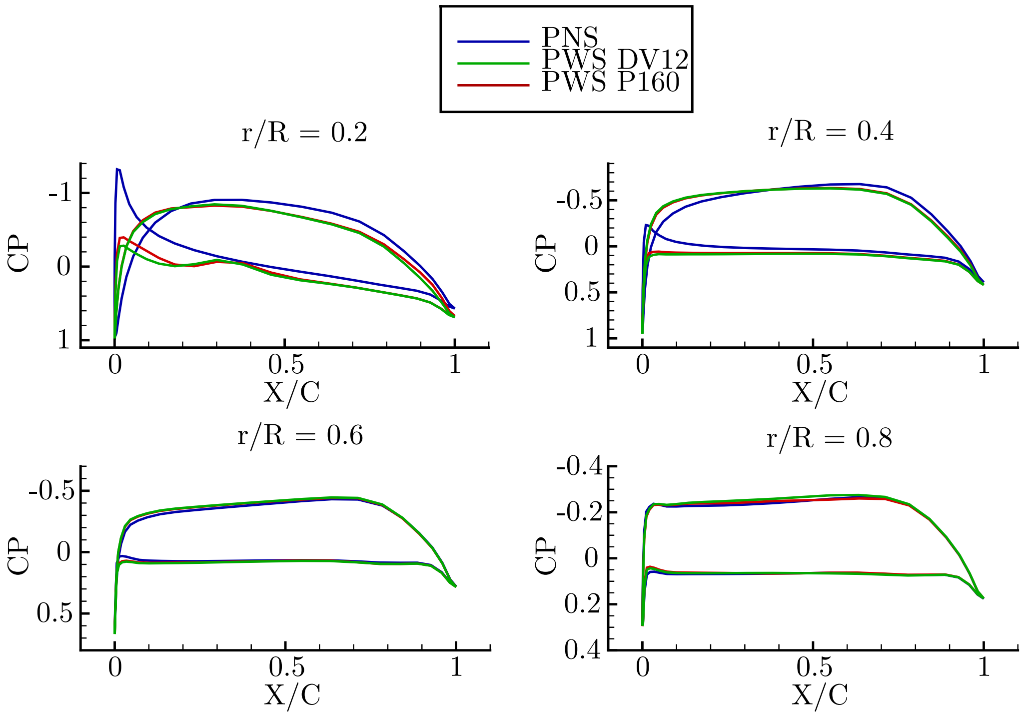

Figure 5.17: Comparison of the chord wise pressure coefficient for different radial stations for the propeller operating without stator (PNS) and with stator (PWS) from both the DV12 and P160 optimisation.

The difference between DV12 and P160 is relative small. Only for r/R = 0.2 on the pressure side, close to the leading edge a difference is visible. Though this difference is small, it does contribute to the pressure difference, which is higher for the DV12. This endorses the increase of the normal force in fig. 5.16 for the DV12 stator relative to the P160 stator.

5.3.2 Stator hydrodynamics

The axial and tangential forces acting on the stator blade and the blade efficiency of the stator, are depicted in fig. 5.18. From the first graph, it can be seen that the stator generally introduces an additional negative force in axial direction, the resistance of the stator. This additional drag has to be overcome by the propeller, this corresponds to the increased thrust generated by the propeller when a stator is added, see table 5.3.

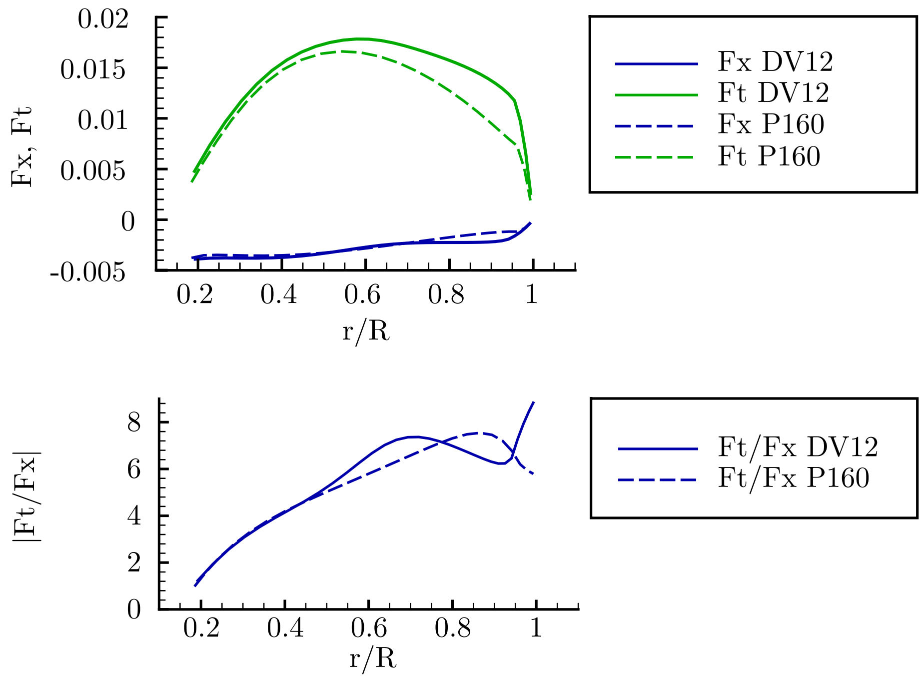

Figure 5.18: Radial distribution of the axial- and tangential force acting on stator (above) and the blade efficiency (below) of the DV12 optimisation compared with the P160 optimisation.

The axial force gradually decreased towards the tip of the blade for both the DV12 and P160 stator. At r/R = 0.8, the decrease stagnates for the DV12 stator before dropping to zero after r/R = 0.95. This result is different from the axial force on the P160 stator, which is lower between r/R=0.85 and r/R= 0.9. This behaviour can be related to the different pitch angles at the tip of these two stators. The pitch angle of the P160 stator is considerable lower at the tip, compared to the DV12 stator pitch angle, which results in a larger (negative) axial force on the blade.

The different pitch angles at the tip are reflected more pronounced in the plot of the tangential forces. Here, the difference of the pitch resulted in a larger (negative) tangential force on the DV12 stator from r/R = 0.45 up to r/R = 0.95.

From the hub, up to half the radius, the blade efficiency of the two stators is practically the same. For the P160 stator, the blade efficiency steadily increases up to r/R - 0.9, to decrease thereafter. The tangential force is relative large compared to the axial force, which means more pre-swirl is generated with less additional drag. The change in blade efficiency over radius of the DV12 stator is different for larger radii. This, again is most likely the effect of the difference of the pitch between the two stator geometries. For r/R = 0.5 till r/R = 0.75, and for r/R > 0.95, the DV12 stator has a relative higher blade efficiency. Here, the generation of pre-swirl is affected more compared to the P160 stator.

To conclude the comparison of the results of the DV12 stator with the P160 stator, an overview of the chord wise pressure distribution at four radial stations is shown, fig. 5.19. The plot for r/R = 0.2 shows the pressure lines crossing close to the trailing edge and a slightly higher pressure on the suction side of the stator blade, compared to the plots for r/R = 0.4 and 0.6. This is in agreement with the lower tangential force at lower radii shown in fig. 5.18. The crossing of pressure lines is a result of an increase of pressure on the suction side towards the trailing edge. Here the flow velocity is reduced, which could be due to the blade geometry, or as a result of the definition of the trailing vortices in the BEM simulation.

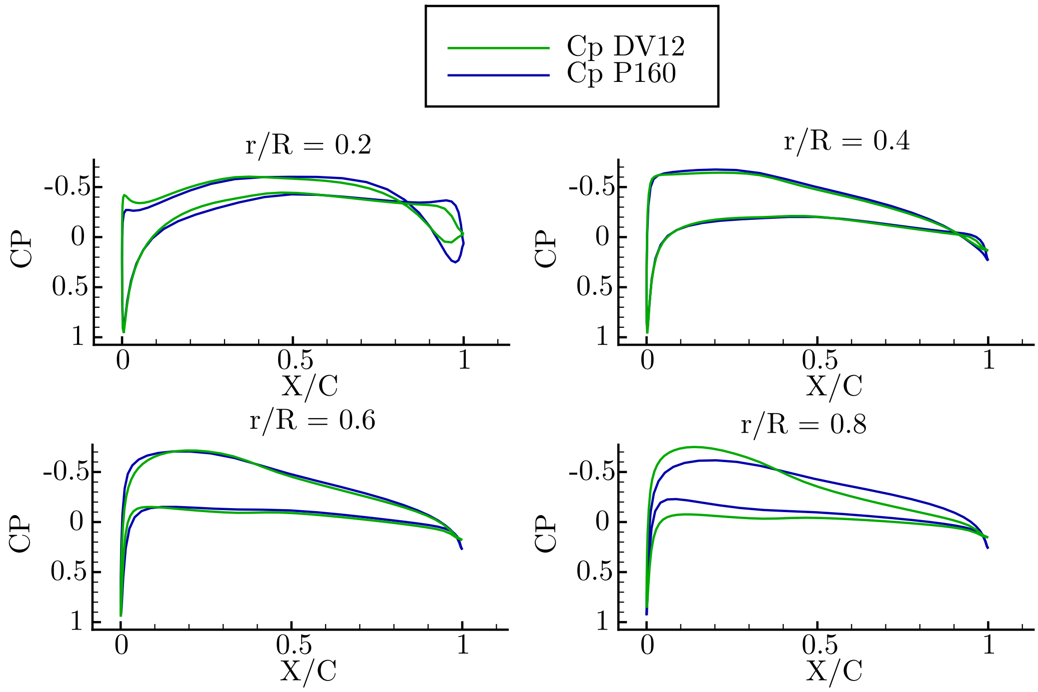

Figure 5.19: Chord wise pressure coefficient acting on the stator for different radial stations of the DV12 stator compared with the P160 stator.

Close to the tip, at r/R = 0.8, the pressure over the DV12 blade is different from the P160 blade. Here, the pressure difference of the DV12 was bigger over the front half of the blade chord and while being is slightly smaller over the aft half of the chord. The surface between the DV12 pressure lines seems slightly larger compared to the P160 lines, which would explain the relative larger tangential force, discussed above.

Next, a short comparison of the results obtained with a BEM simulation with results from a RANS simulation will be given.

5.4 Comparison BEM simulation with RANS

In the optimisation process, the simulation of the stator and propeller are both performed with a BEM solver; the BEM-BEM coupling. The quality of the stator simulations was evaluated by doing a RANS simulation of the stator coupled to a BEM simulation of the propeller; the RANS-BEM coupling. The results of these simulations are presented in this section.

The set-up of the RANS simulations is not part of this research and was done by Bart Schuiling, researcher at Marin. The simulations were performed with the viscous flow solver ReFRESCO. Solutions of these simulations where converged sufficiently to do an energy analysis on the stator and to asses the results for comparison with the BEM solution.

5.4.1 Stator geometry

The stator geometry used in this comparison is based on the winning geometry of the P160 optimisation, presented in section 5.1. The geometry, shown in fig. 5.20, has a comparable pitch and chord distribution, while the chamber is changed. For this stator it was chosen to have a constant chord over the radius. Since the DV6 optimisation showed that the chord did not have much influence, it was decided that a constant chamber would be more suitable, in order to keep the blade geometry more simple. The radial distribution of the three design parameters are shown in fig. 5.21

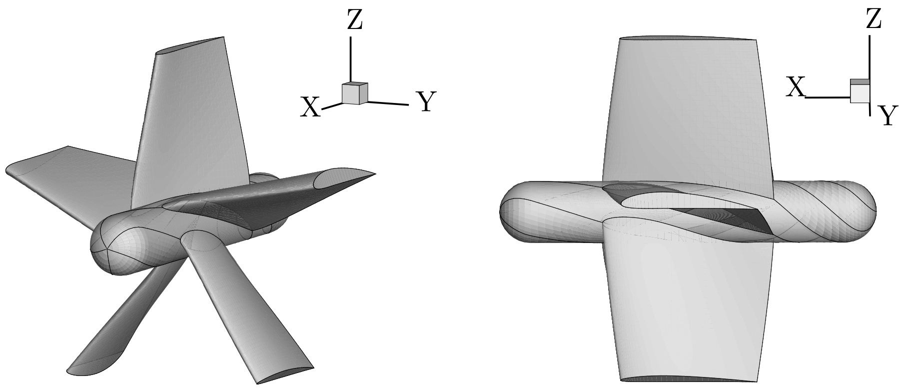

Figure 5.20: Stator geometry used to compare results of the RANS simulation with the results of the BEM simulation.

5.4.2 Efficiency analysis

The stator efficiency was determined for both the BEM-BEM and the RANS-BEM simulations. In table 5.6 the propeller performance is listed for both simulations and the performance of the propeller without stator (PNS).

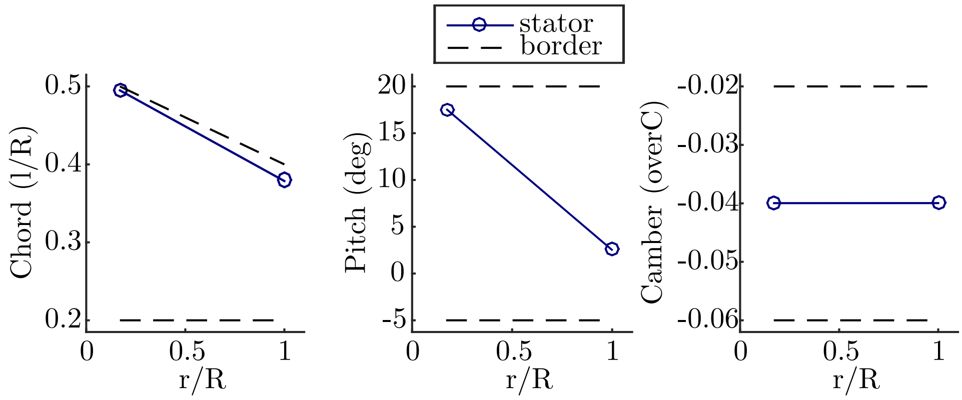

Figure 5.21: Parametrisation of the chord, pitch and chamber, used to define the stator geometry used in the RANS simulation.

Table 5.6: Propeller performance of RANS-BEM coupling simulation versus BEM-BEM coupling.

			BEM	RANS	PNS
Propeller rotation rate	n	rps	1.002	0.983	1.083
Thrust	T	kN	631.1	649.0	599.0
Torque	Q	kNm	650.8	643.3	620.6
Power	P	kW	4097	3973	4223
Power percentage of PNS	P	%	97.02	94.08	–

With the inclusion of viscous effect in the simulation, the resistance of the stator increased while the torque decreased, relative to the inviscid simulation. Though the generated thrust is higher in the RANS simulation, the rotation rate of the propeller was lower. This resulted in a considerably lower power with 94.08% reduction, compared to the BEM simulation with a reduction of 97.02%, relative to the propeller operating without stator. The resulting increase in efficiency is determined with the efficiency analysis presented in section 2.2.2. In fig. 5.22, the changes in efficiency due to the stator are depicted for both the BEM and RANS simulations.

The reduction of the rotation rate is the biggest contribution to the efficiency gain with the stator, causing the blade loading efficiency to change. As mentioned above, the rotation rate of the propeller in the RANS simulation was lower than in the BEM simulation, which improved the blade loading efficiency by 10.2% and 7.5% respectively.

In the BEM simulation, the change in blade efficiency was much lower with an improvement of 0.9%, while in the RANS simulation, the blade efficiency was changed with 4.5%. In the BEM simulation, both torque and thrust increased almost evenly, while in the RANS simulation, the increase of the torque was lower compared with the increase of thrust which has a positive on the change of the blade efficiency.

The higher added resistance of the stator in the RANS simulation caused the interaction efficiency to reduce. The stator has a larger resistance in the RANS simulation than in the BEM simulation, which reduces the change interaction efficiency of the stator.

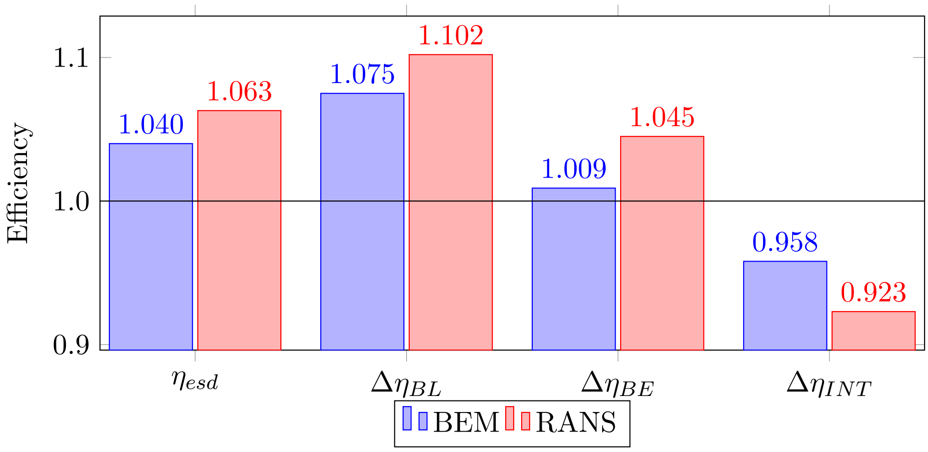

Figure 5.22: Bar diagram with results of the efficiency analysis to compare BEM with RANS results.

Overall, the stator efficiency was higher for the RANS simulation. The stator increased the propulsive efficiency of the propeller with 6.3% versus 4.0% in the BEM simulation. In order to get a better image of the difference between the BEM and RANS simulations, the resulting flow field behind the stator will be compared, as well as the forces and pressure on the stator.

5.4.3 Hydrodynamic comparison BEM and RANS simulation

The resulting tangential velocities behind the stator are plotted in fig. 5.23. The pre-swirl generated in the two simulations is globally the same, however, a close inspection shows some small differences. In the RANS simulation, the rotation rate is slightly higher close to the hub, which could be one of the reasons for the higher stator efficiency in the RANS simulation. Towards the tip, the area of positive wake rotation was slightly larger in the RANS simulation as well. However, the added tangential velocity is small here, while the influence of the stator on the tip is small compared to the hub region(section 2.2), hence this difference is negligible.

Figure 5.24 shows two contour plots of the axial velocities behind the stator for both the BEM and RANS simulations. What catches the eye, is the difference in velocity between both simulations. In the BEM simulation, the axial velocity was reduced slightly, while in the RANS simulation this effect was much larger. Especially close to the hub, the reduction of the velocity was much more pronounced. This is a positive effect for the propeller, which can induce a larger velocity difference, without inducing extra axial losses in the wake. Also the angle of inflow is changed favourable this way. In the RANS, the velocity is reduced more due to the viscosity: the resistance of the stator slows down the flow. In the BEM simulations this effect is not accounted for during the calculation of the velocities and hence the flow is only slowed down due to the changes in direction of the absolute velocity vector.

Figure 5.25 shows the axial- and tangential forces over the stator radius, together with the blade efficiency. The difference between the axial forces in the BEM and RANS reflects the difference in thrust seen in table 5.6. Close to the hub, the resistance is

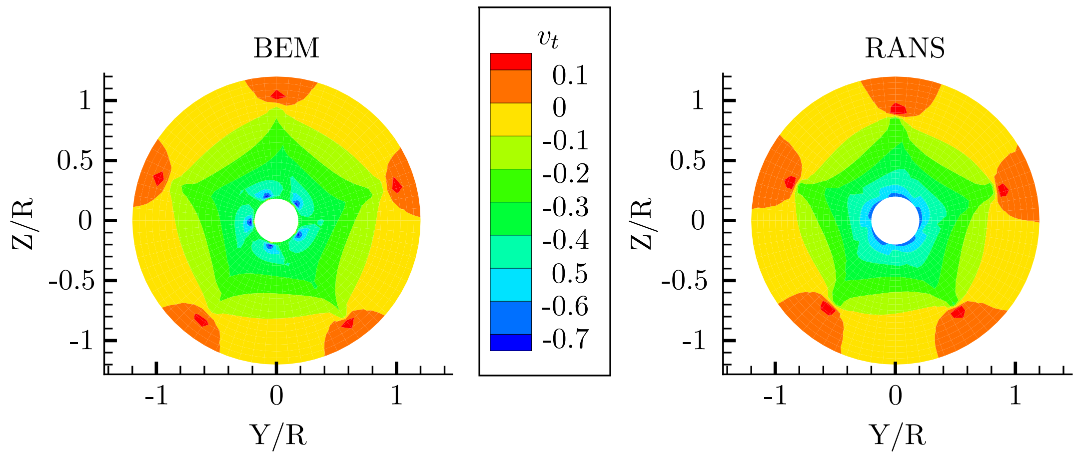

Figure 5.23: Countour plots of the tangential velocity behind the pre-swirl stator, simulated with the BEM code and the RANS code.

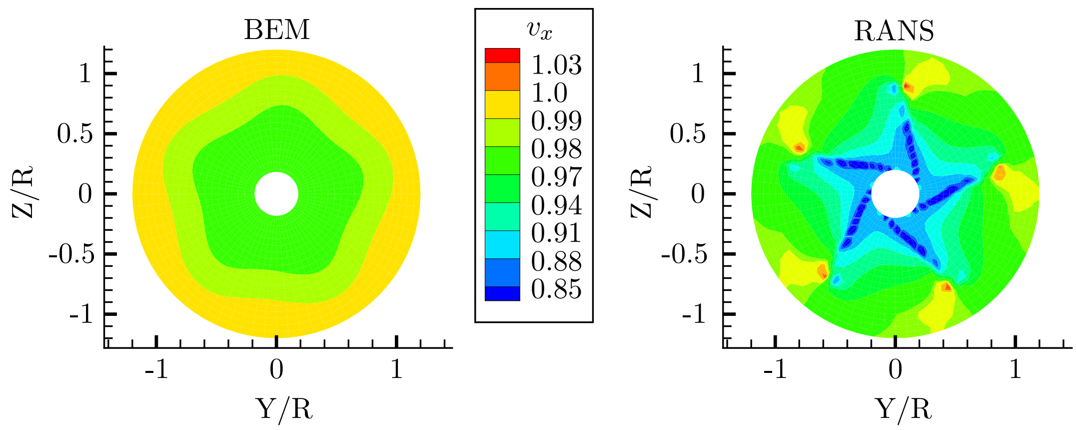

Figure 5.24: Countour plots of the axial velocity behind the pre-swirl stator, simulated with the BEM code and the RANS code.

considerably lower in the BEM simulation, compared to the RANS. Also the tangential force on the stator is larger in the RANS simulation, i.e. both lift and drag are increased when viscous effects are taken in to account.

Though the efficiency of the stator in the RANS simulation was higher, the blade efficiency of the resulting blade efficiency was lower. The added viscosity increases the resistance of the stator, which in turn has a negative effect on the blade efficiency.

The pressure on the stator over the blade chord is plotted for six radial stations in fig. 5.26. Here, a large difference can be seen between the BEM and RANS simulations. The pressure on the stator in the BEM simulations increased towards the trailing edge, while this was not the case in the RANS simulation. The reason for this can be found in the coupling procedure. In the BEM simulation, only the effective wake field is transferred between the stator and propeller simulation. Any change of pressure at the stator surface, as result of the operating propeller, is not taken in to account. As depicted in fig. 5.27, the pressure decreases considerably over the stator chord. In the RANS simulation, this pressure gradient is incorporated.

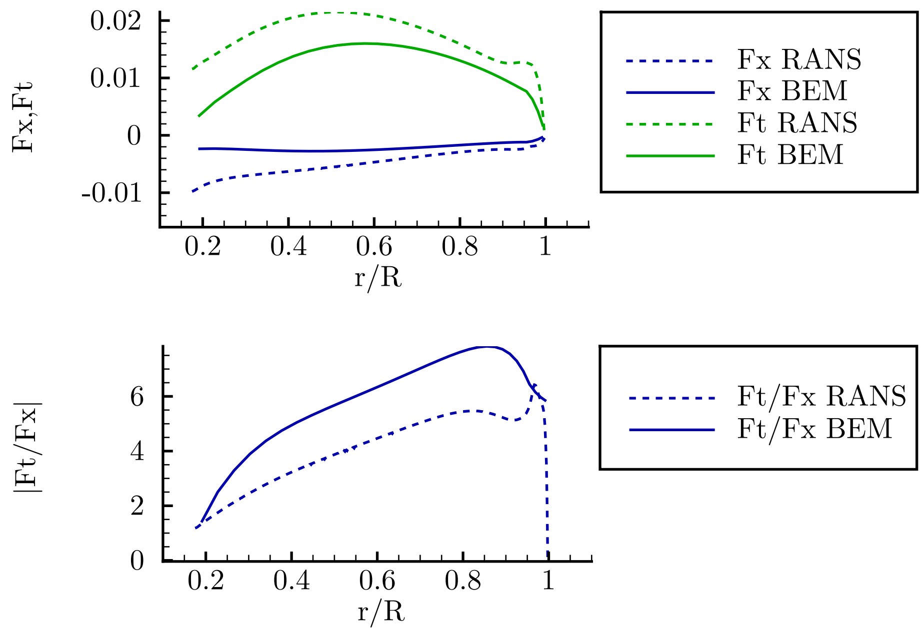

Figure 5.25: Radial distribution of the axial- and tangential forces on the stator and the resulting blade efficiency. Plotted for both the BEM and RANS simulation.

Further more, the stator in the BEM simulation showed a crossing of the streamlines close to the trailing edge. This effect was negligible in the RANS simulations, which had a positive contribution to the lift. Also, the pressure difference decreased less over the chord in the RANS simulation, especially for the higher radial stations.

Concluding, the BEM simulation misses an important effect not taking into account the reduction of pressure due to the operating propeller. This is most likely the reason for the axial and tangential forces on the stator being lower, which, in turn reduces the pre-swirl generating effect and hence in a lower efficiency improvement. Further research should prove whether or not this is true.

In general, the results of both the RANS and BEM simulations showed comparable results in the calculation of the tangential wake field velocities and both simulations found a positive change of the propulsive efficiency of the propeller with stator.

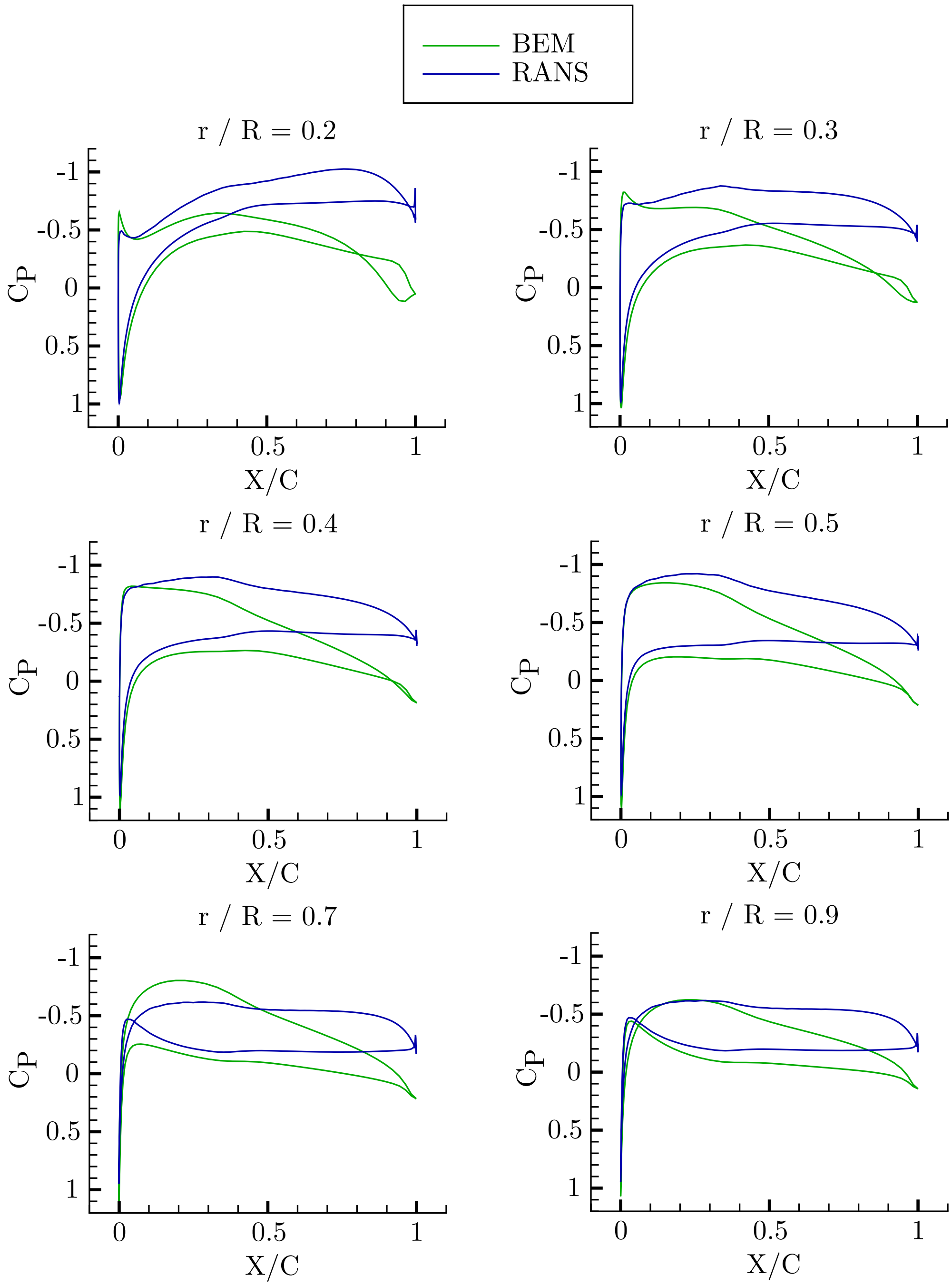

Figure 5.26: Plot of the chord-wise pressure distribution on the stator blade, at six radial stations, given for the BEM and RANS simulation.

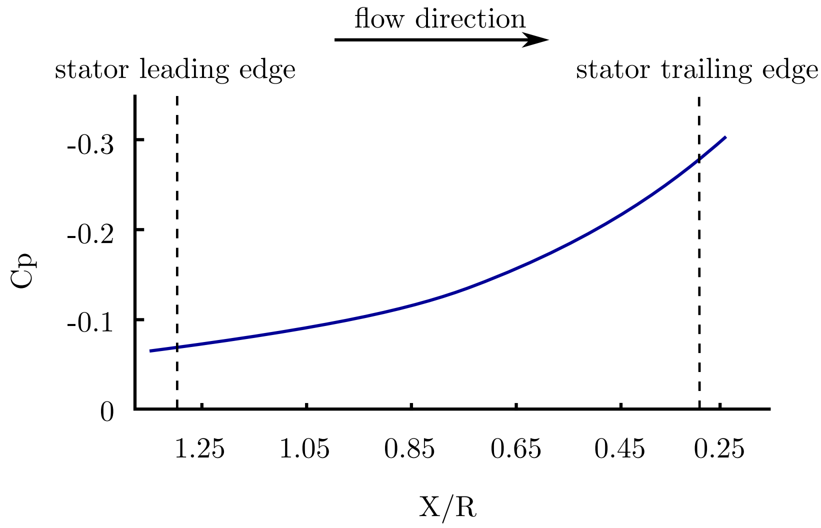

Figure 5.27: Plot of the total pressure in front of the propeller, simulated in open water with a RANS code.

Chapter 6

Conclusions and recommendations

The research presented in this thesis aimed to develop an optimisation tool for pre-swirl stator designs, in order to lower the required energy to propel a ship. This chapter presents the conclusions of this research. In order to improve in the future, some recommendations are given as well.

6.1 Conclusions

First, the effect of a pre-swirl stator on the propulsive performance of a propeller was studied. Addition of pre-swirl to the wake alters the angle of inflow at the propeller blade. An increase of this angle can lead to a favourable change of the force vector on the propeller blade, which increases propeller performance by reducing rotational losses in the wake. Then, in order to maintain a constant speed, the rotation rate has to be reduced, which reduces the required power and hence increases the propulsive efficiency. To change the angle of inflow at the propeller blade, the velocity induced by the stator has most influence at the lower radii of the propeller since rotational losses are the largest here. This should be taken in to account when designing a stator.

Second, a suitable optimisation routine was sought within the available software at Marin. It was decided to perform optimisations with a genetic algorithm in Dakota. Dakota offers a broad range of optimisation algorithms and analytic tools and can be coupled to any simulation tool. With a genetic algorithm, it is possible to optimise for multiple objectives, though tested for a single objective only in this research. With 6 optimisation parameters, the optimisation converged within 21 generations with a solution that reduced the propulsive power by 5.3%. The test case optimisation with 12 parameters did converge as well, however, the response was still decreasing in the last population indicating the final optimum had not been reached jet.

And third, the design parameters involved when designing a pre-swirl stator were investigated. In the test cases, chord, pitch and chamber were varied with different parametrisation. Parameter studies showed that the pitch at the hub and tip of the stator blade were the most important design parameters, followed by the chord at the hub. The influence of the chamber was of negligible influence within the given design range. Other design parameters to vary are the number of stator blades, the position of the stator blades with respect to the propeller and the thickness. These parameters were not tested, and more research is needed.

This lead to the answer on the main question in this thesis, as posed in section 1.2:

How can MARIN's numerical simulation tools be merged into an optimisation frame-work for pre-swirl stators, in order to lower the required power of a ships propeller operating in open water?

The optimisation tool developed in this research proved to be capable of optimising the design of pre-swirl stators in combination with a propeller operating in open water. Simulations are performed with a Boundary Element Method (BEM), which solves simplified flow equations but creates an accurate model of the flow around both stator and propeller. The coupling of the stator and propeller converges within six iterations, which proved that the influence of the induced velocities of both the pre-stator and propeller is relative small.

Comparison of the Boundary Element Method simulation with a Reynolds Averaged Navier-Stokes (RANS) simulation showed an important difference in the resulting pressure on the pre-swirl stator. Since the RANS simulations use more detailed flow equations, results from these simulations are more accurate. This would mean that the BEM simulations results under-predict the actual improvement of the propulsive efficiency of a pre-swirl stator. This can be solved by incorporating the pressure gradient over the stator blades, due to the rotating propeller, in the BEM-BEM coupling simulations.

In summary, the optimisation tool combines fast simulations with Marin's BEM code Procal with a genetic algorithm that is capable of handling multiple optimisation parameters and objective functions. The resulting stator design reduce the propulsive power by 5.4-6.5% in open water. This optimisation tool returns an optimal solution within a matter of days without designer interaction. This is a great advantage compared to manual simulating different stator designs. This reduces the costs of the design process, making this energy saving device more attractive for shipping companies.

6.2 Recommendations

The optimisation frame-work presented in this thesis, is merely a proof of concept. The complexity of the test cases was kept relative low to test the process first and to find suitable means of interpreting the results. In order to improve the optimisations further, several recommendations are given.

- Improve the codes and define clear input files. The optimisation process contains several codes to link the simulations performed in Procal to the optimisation software of Dakota. Over time these codes have grown and the perception of how to couple certain modules changed. Revising the code can reduce to changes of errors during optimisation and will improve the ease of using the optimisation tool.

- Incorporate the pressure gradient in front of the propeller in the stator simulations. Doing this, the coupling simulations should give a more realistic result.
- Test the optimisation routine with other design variables and different design ranges. The number of blades, their location with respect to the propeller and the blade thickness was kept constant though they are important parameters in the stator design. Also the optimisation routine should be tested for in behind conditions.
- The stator design is not checked for its strength, possible vibrations of manufacturability. This should be investigated further and if needed incorporated in the optimisation process by, for example, defining certain boundaries or relations between optimisation parameters.
- Add reduction of the rotational kinetic energy flux left in the wake as an optimisation objective. Pre-swirl is most effective when applied for lower radial sections of the propeller. Pre-swirl at higher radial sections does not necessary influence the propulsive power, while it will induce rotation which is left in the wake. Optimising for minimal rotational kinetic energy flux should reduce this effect.

Bibliography

[1] Intership Navigation, 2008, *MCP Class*, [online] http://www.intership-cyprus.com/mcp-class [date accessed 2016-11-25].

[2] United Nations, 2015. Review of maritime transport, *United Nations Conference on Trade and Development*, ISBN 978-92-1-112892-5.

[3] P. Papalambros, D. Wilde, 2000. *Principles of Optimal Design Modeling and Computation (second edition)*, Cambridge: Cambridge university press, ISBN 978-0-521-62727-6.

[4] B. Schuiling, T. van Terwisga, 2015, Hydrodynamic Working Principles of Pre-Ducts in Ship Propulsion Systems, *GRIP*.

[5] Website Shipping Efficiency, 2016. *Fuel savings calculator*, [online] http://shippingefficiency.org/fuel-savings-calculator [date accessed 2016-10-31].

[6] T. van Terwisga, 2013. On the working principles of Energy Saving Devices, *Third International Symposium on Marine Propulsors SMP'13*.

[7] B. Schuiling, T. van Terwisga, [-]. Computational Energy Analysis of a Propeller in Open Water, *Yet to be published*.

[8] B. Schuiling, T. van Terwisga, 2016, Hydrodynamic working principles of pre-ducts in ship propulsion, *GRIP*.

[9] T. Burton, N. Jenkins, D. Sharpe, E. Bossanyi, 2011. *Wind Energy Handbook*, Wiley: ISBN 978-0-470-69975-1.

[10] J Carlton, 2012. *Marine Propellers and Propulsion*, Elsevier: ISBN 978-0-08-097123-0.

[11] Dakota website, 2016. *Dakota*, [online] https://dakota.sandia.gov [date accessed 11-10-2016].

[12] B.M. Adams, M.S. Ebeida, M.S. Eldred, et al, 2014. *Dakota, A Multilevel Parallel Object-Oriented Framework for Design Optimization, Parameter Estimation, Uncertainty Quantification, and Sensitivity Analysis: Version 6.4 Users Manual*[pdf] Available at https://dakota.sandia.gov/documentation.html [date a accessed 05-12-2016].

[13] CRS website, 2016. *Cooperative Research Ships Home*, [online] http://www.crships.org/web/show/id=122123/langid=42 [date accessed 11-10-2016].

[14] J. Bosschers, 2015. *User's Guide PROCAL Baseline code version 2.221*, Marin internal document.

[15] N. P. Kruyt, 2013. *Lecture Notes Fluid Mechanics of Turbomachines II*, Enschede: University of Twente.

[16] L. Eça, G. Vaz, M. Hoekstra, 2010. A Verification and Validation Exercise for the Flow Over a Backward Facing Step, *European Conference on Computational Fluid Dynamics*.

[17] E. Rotteveel, A. van der Ploeg, R. Hekkenberg, 2016. Optimization of Ships in Shallow Water With Viscous Flow Computations and Surrogate Modelling, *PRADS*.

[18] E Foeth, 2015. Propeller Optimization Using an Unsteady Boundary-Element Method, *Fourth Interantional Symposium on marine Propulsors*, Austin Texas.

[19] LeanShips website, 2016. *Demo Case Large Diameter Propeller for General Cargo Vessel*, [online] http://www.leanships-project.eu/demo-cases/demo-case-09/overview/ [date accessed 11-10-2016].

[20] Consultancy Services Group, Technical Investigations, 2005. *PROCAL panneling procedure*, Report Number 6517 Marin internal document.